Technical developments for *in vivo* electrical property mapping using magnetic resonance imaging

Narae Choi

The Graduate School
Yonsei University

Technical developments for *in vivo* electrical property mapping using magnetic resonance imaging

A Dissertation

Submitted to the Department of Electrical and Electronic Engineering

and the Graduate School of Yonsei University

in partial fulfillment of the

requirements for the degree of

Doctor of Philosophy

Narae Choi

February 2015

This certifies that the dissertation
of Narae Choi is approved.

_____
Thesis Supervisor: Dong-Hyun Kim

_____
Donghyun Kim

_____
Dosik Hwang

_____
Hyunyong Choi

_____
Hyung Joong Kim

The Graduate School
Yonsei University
February 2015

감사의 글

이 논문은 저를 도와주신 분들이 없었다면 완성될 수 없었을 것입니다. 연구실에 들어와 졸업할 때까지 많은 분들의 도움을 받았습니다.

가장 먼저 MRI 분야에서 다양한 연구를 할 수 있도록 지도해주신 김동현 교수님 감사 드립니다. 학위과정 동안 길을 잃지 않도록 늘 이끌어주시고 격려해주셔서 연구자로서의 저로 성장할 수 있었습니다. 교수님의 늘 더 멀리 넓게 생각하시는 모습을 보며 저도 닮고자 노력하였습니다. 연구자로서 아직 가야 할 길이 멀지만 앞으로도 열심히 연구해서 교수님 같은 연구자가 되고 싶습니다. 늘 건강하시길 바랍니다.

학위논문 심사를 맡아주신 본교의 김동현 A 교수님과 황도식 교수님, 최현용 교수님, 그리고 경희대학교의 김형중 교수님께 감사 드립니다. 바쁘신 와중에도 심사를 맡아주신 김동현 교수님 감사 드립니다. 교수님의 말씀을 통해 논문의 흐름이 명확해 졌으며 구조를 바로 세울 수 있었습니다. 일정을 맞추기 어려운 와중에 많은 배려를 해주신 최현용 교수님 감사 드립니다. 교수님의 칭찬과 지지로 큰 힘을 얻었습니다. 심사기간에 먼 길을 와주신 김형중 교수님께 감사 드립니다. 교수님의 꼼꼼한 조언으로 더욱 풍요롭고 완성도 높은 논문을 작성할 수 있었습니다. 심사뿐 아니라 과제를 함께 수행하며 연구지도 및 많은 조언을 해주신 황도식 교수님께 감사 드립니다. 과제를 진행하시는 모습을 보며 새로운 시각으로 과제를 바라볼 수 있었고 많은 것을 배울 수 있었습니다. 항상 제 연구에 관심 가져 주시고 격려해주셔서 감사합니다.

연구실에서 함께 생활하며 많은 도움을 준 선후배 동료들에게 감사 드립니다. 연구실에 들어와서 선배님들께 많은 도움을 받았습니다. 열정적으로 연구하며 놀라운 실력으로 연구실의 여러 연구도구들을 남겨준 상영오빠, 저를 포기하지 않고 시퀀스의 기틀을 가르치고 함께 졸업준비 하면서 많은 의지가 되었던 한성오빠, 신입생 때부터 비슷한 주제로 연구하며 연구실 생활을 더 다채롭게 만들어준 성민오빠께 감사 드립니다. 평소 고민상담 및 연구 질문에도 늘 좋은 대답을 해주던 윤호오빠, 항상 열심히 연구하고 잘하며 연구에 많은 도움을 주는 완벽한 민오오빠에게 감사 드립니다. 함께 입학한 동기여서 더 든든하고 힘이 되었습니다. 연구실 생활하며 많은 의지가 된 더 함께하지 못해 아쉬운 어른스럽고 든든한 은혜 꼭 연구에서 좋은 성과 내길 바라고, 막내생활 오랫동안 하면서 연구실의 궂은일도 많이 하고 영어도 많이 도와준 승욱이, 연구에 큰 도움을 주시며 지도해주신 이준성 박사님께 감사 드립니다. 열정적으로 연구하는 든든한 동엽이 박사생활도 즐겁게 하길 바라고, 묵묵하게 꾸준히 연구하며 늘 겸손한 재욱이 먼저 가서 기다릴게. 열심히 하며 맡은 일을 해내는 홍표, 잠시 동안이었지만 함께해서 즐거웠던 신국이, 똑똑하고 유쾌하며 성실한 한솔이, 어려운 실험도 열심히 잘 해내는 (조)성민이,

잠재력이 무궁무진할 것 같은 태화, 여러 어려움에도 불구하고 함께 어울리려 노력하는 Saeed, 앞으로 좋은 모습 보여줄 것 같은 준형이와 재은이까지 함께해서 감사했고 든든했으며 많은 도움을 받았습니다. 모두 연구하는 분야에서 빛나는 사람이 되길 바랍니다. 잠시나마 함께했던 박재석 교수님 연구실의 현열, 수영오빠와의 연구 교류로 많은 도움을 받았습니다. 함께 과제 진행했던 황도식 교수님 연구실의 장진성, 어태준에게도 감사를 전합니다.

고민이 있을 때마다 함께해주고 연구질문에도 귀찮아 하지 않고 고민해주던 열정적이고 능력 있는 멘토 같은 세정언니, 친 오빠 같은 형종오빠, 서문 길동무 일영오빠, 항상 저를 아껴주는 선옥언니 감사드립니다. 늘 곁에서 응원해주고 지지해주는 보남이, 정균오빠, 소연이, 지연이, 주원이, 상헌이, 선영이, 그리고 항상 변화의 기회를 주며 내편이 되어주는 피터에게 감사인사 전합니다. 일일이 다 나열하지 못한 항상 주변에서 힘이 되고 격려가 되는 저의 선배 후배 동기 친구들에게 감사의 말씀들 드립니다.

마지막으로 제게 너무나 큰 사랑을 주시는 아버지, 어머니께 감사의 말씀을 드립니다. 제게 좋은 면이 있다면 대부분 부모님으로부터 물려받은 것일 겁니다. 항상 저를 믿고 아낌없이 지지해주셔서 학업에 전념할 수 있었습니다. 앞으로도 늘 건강하고 행복하시길 바랍니다. 그리고 룸메이트이자 사랑하는 동생 단비에게 감사를 전합니다. 때로는 언니처럼 채찍질 해주고, 때로는 친구처럼 내 편이 되어주며 항상 함께해줘서 큰 의지와 위안이 되었습니다. 어디에서도 당당하고 멋진 사람이 되길 바랍니다.

2015 년 1 월

최나래

Content

List of figures

List of tables

Abstract

Technical developments for in vivo electrical property mapping using magnetic resonance imaging

Narae Choi

Dept. of Electrical and Electronic Eng.

The Graduate School

Yonsei University

Magnetic resonance imaging (MRI) is a widely used technique for diagnosing disease. Recently, MR-based electrical property mapping was proposed as a new imaging modality which provides unique contrast information of human body. This dissertation is related to the study of in vivo electrical property using MRI. Specifically three studies are presented in this thesis: 1) a technique for mapping the electrical properties is presented, 2) a novel contrast imaging scheme using the electrical properties is developed, and 3) an application focused on measuring the conductivity of blood is presented. In the first study, a gradient echo based double-angle multi-echo actual flip-angle imaging sequence (DA-AFI) was developed for MR image acquisition and a B_1^+ mapping technique was proposed to simultaneously calculate the complex B_1^+ map. This proposed method is robust to the noise comparison with the conventional AFI. In the second study, using the previously developed B_1^+ map, loss tangent imaging was proposed as a supplementary tool for estimating the thermal sensitivity of tissues. Simulation analysis showed the potential of loss tangent imaging to be a tool for

predicting the RF wave propagation in the context of hyperthermia. Using conventional processes, there was limitation that the phase information of the B_1^+ is frequently distorted due to the flow components. The third study focused on correcting this distortion. Since flow effects were hard to remove using conventional methods, a double spin echo was used to compensate the flow effect. To improve the estimation of electrical conductivity of flow components, the flow induced effects in B_1^+ phase was analyzed with a velocity map. These approaches were studied with phantom and *in vivo* experiments. In summary, the proposed methods estimated *in vivo* electrical properties non-invasively and enhanced the robustness of the estimation by developing new pulse sequence for MR image acquisition and technique for post-processing algorithm.

Keywords: magnetic resonance imaging, B_1^+ mapping, electrical property mapping, MREPT, loss tangent imaging, flow effect removal

Chapter 1
Introduction

1.1 MRI basics

Magnetic resonance imaging (MRI) is a versatile tool and widely used technique for diagnosing disease. MRI provides high resolution anatomical information, excellent soft tissue contrast of the human body with non-invasive manner, and can obtain various contrast information such as proton density image, T_1-weighted image, T_2-weighted image, and susceptibility weighted image. Recently, MR-based electrical property mapping was proposed as a new imaging technic which provides unique contrast information [1-3]. Electrical property mapping enables imaging of quantitative conductivity and permittivity maps.

The rest of this chapter is outlined to provide background knowledge in understanding electrical property imaging using MRI.

1.1.1 Magnetic polarization

Water is a major component of human body. Most of the MR imaging uses the interaction between hydrogen in the water (proton or ^{1}H) and electromagnetic field. Inside a strong static magnetic field, usually referred to the main field B_0, a net magnetization $\vec{M}$ in the direction of B_0 is formed. The net magnetization $\vec{M}$ is a source of MR signal.

The net magnetization $\vec{M}$, which is formed spins having intrinsic angular momentum, can be described as a spinning gyroscope. If the $\vec{M}$ is tipped away from applied B_0 field, $\vec{M}$ will precess along the main magnetic field with a specific resonance frequency. This frequency called Larmor frequency is defined with the following equation

$$\omega_0 = \gamma B_0 \quad \text{(rad/s)} \tag{1.1}$$

where ω_0 is the Larmor frequency and γ is the gyromagnetic ratio. The gyromagnetic ratio is a constant which is characteristic of the nucleus. In water, the hydrogen has a gyromagnetic ratio of 2.675×10^8 rad/s/Tesla or 42.576 MHz/Tesla. In this thesis, all images are obtained from the magnetization of hydrogen (^{1}H) with a magnetic field strength of 3 Tesla which corresponds to a Larmor frequency of approximately 128 MHz.

Figure 1.1 illustrates the magnetization and precession of nuclear spin in the applied magnetic field B_0 (z direction). Using a classical physics perspective, the protons are aligned parallel and anti-parallel to the main magnetic field. The difference in the number of them, which is determined by the Boltzmann distribution, forms the net magnetization $\vec{M}$.

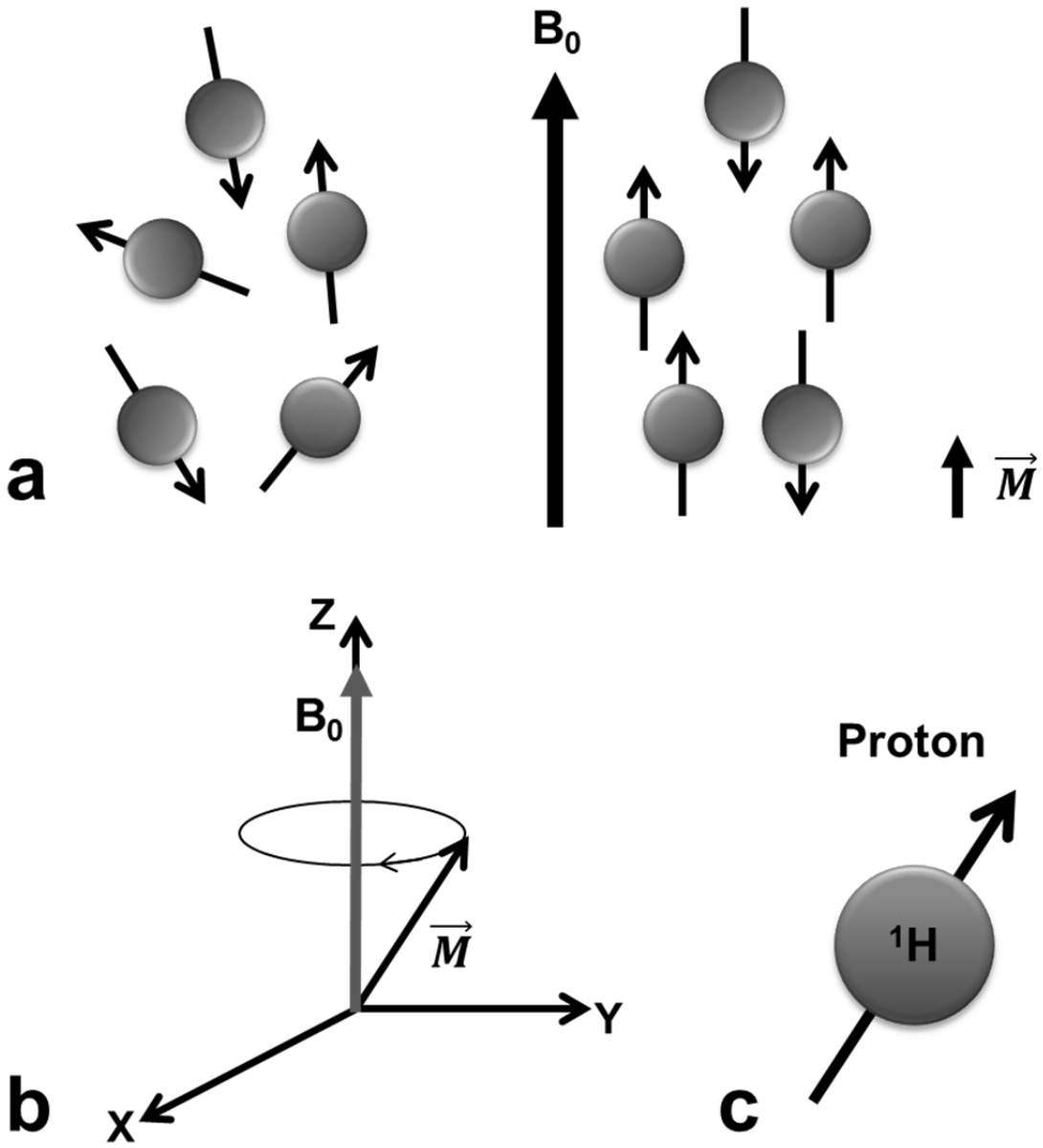

Figure 1. 1 Spin models to describe the behavior of protons when the B_0 is applied. **a**. After magnetic field B_0 is applied, randomly distributed protons are aligned to B_0. **b**. The net magnetization $\vec{M}$ precesses with Larmor frequency along B_0 direction (z direction). **c**. A simplified spin model of proton (hydrogen nucleus ^1H).

1.1.2 Excitation

In equilibrium state, $\vec{M}$ stays in the main field direction (z direction) while the transverse component (xy direction) is zero. $\vec{M}$ can rotate away from the z direction by applying an external magnetic field. This external magnetic field that is applied is called RF (radiofrequency) excitation field and the resulting magnetic field that is produced is referred to as the $\overrightarrow{B_1}$ field. To change the aligned axis of spin, the RF excitation pulse should rotate in the same manner as the precessing spins. This is known as resonance condition [4]. By convention, the magnetization is said to rotate in the counterclockwise direction (Fig. 1.1).

$\overrightarrow{B_1}$ field is typically applied with a short duration (a few milliseconds) and oscillates in the radio-frequency range with weak amplitude (about 50mT). Recent MRI systems use quadrature RF transmitter coils to generate $\overrightarrow{B_1}$ field rotating counterclockwise since the net magnetization vector precesses counterclockwise [5]. Circularly polarized field (B_1^+ field) has the advantage of reduced RF power to achieve excitation compared to linear polarization. The B_1^+ field can be represented with following equation

$$B_1^+(t) = \frac{B_{1,x}(t) + iB_{1,y}(t)}{2} \tag{1.2}$$

where $B_{1,x}$ and $B_{1,y}$ are x and y axis components of $\overrightarrow{B_1}$, respectively. Figure 1.2 describes the excitation procedure from a rotating frame view.

After applying $\overrightarrow{B_1}$ field, the spin systems return to the equilibrium state which is called relaxation. The transverse magnetization exponentially decays with a time constant T_2 and the longitudinal magnetization exponentially increases back to the steady state with time constant T_1. The time rate of change of magnetization during precession generates an induced voltage by Faraday's law of electromagnetic induction and this is detected through a receiver coil.

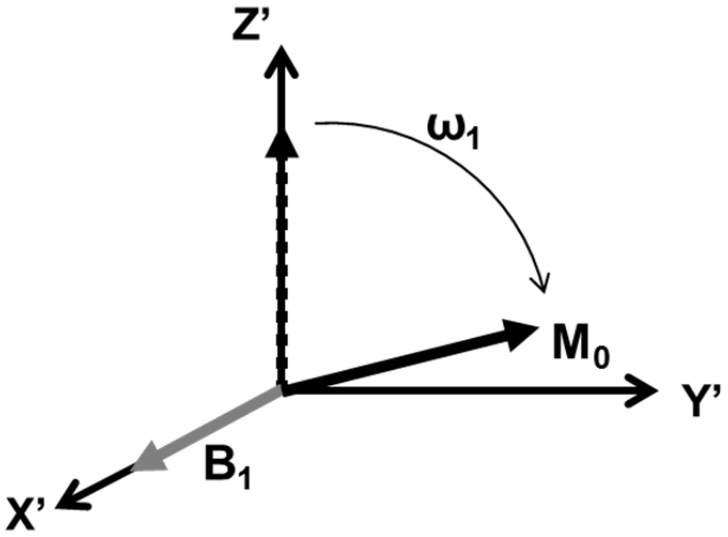

Figure 1. 2 The magnetization is tipped away from the z-axis by applying external magnetic field ($\overrightarrow{B_1}$ field). The axis represents the rotating frame (x', y', z') which rotates around the main magnetic field B_0 with the frequency of ω_0.

1.1.3 B_1^+ and B_1^-

In the presence of an object, the actual magnetic field distribution can be decomposed into B_1^+ and B_1^-components. The B_1^+ field rotates in the same direction as the precessing spins and enforces the excitation of spins. B_1^- field rotates in the opposite direction of the precession direction and produces negligible effects on a spin system. Therefore, the effective B_1 field is considered to be B_1^+.

Figure 1.3 shows simulation result of electromagnetic field distribution for a RF coil which produces a counterclockwise $\overrightarrow{B_1}$. Both B_1^+ and B_1^- are produced in the presence of an object. Although the magnitude of the B_1^- is scaled up five times, the intensity is smaller than B_1^+. From simulation, the magnitude intensity of the B_1^+ is 100 times higher than that of the B_1^- at the center of an object.

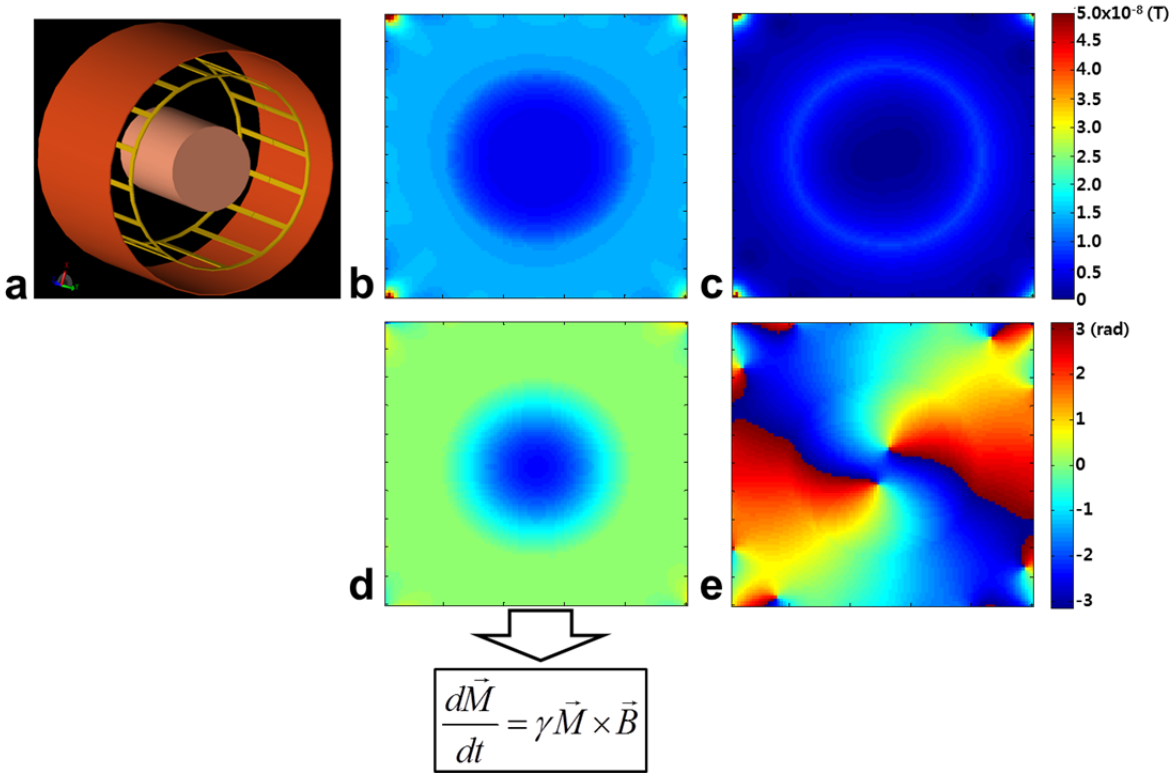

Figure 1. 3 Simulation results. **a.** Phantom model. **b.** B_1^+ magnitude. **c.** $5\times B_1^-$ magnitude. **d.** B_1^+ phase. **e.** B_1^- phase. B_1^+ field which rotates in the same direction of the precessing spins affects the spins to tip along the transverse direction.

1.1.4 The Bloch equation

The behavior of the net magnetization $\vec{M}$ is described by the Bloch equation. The Bloch equation is defined as follows

$$\frac{d\vec{M}}{dt} = \gamma \vec{M} \times \vec{B} - \frac{M_x \vec{i} + M_y \vec{j}}{T_2} - \frac{(M_z - M_z^0)\vec{k}}{T_1}. \qquad (1.3)$$

where $\vec{M}$ = (M_x, M_y, M_z) is the magnetization, $\vec{B}$ = (B_x, B_y, B_z), and M_z^0 corresponds to the equilibrium magnetization. The longitudinal relaxation time (T_1) and transverse relaxation time (T_2) are time relaxation constant which are dependent on tissue characteristic. During the presence of a $\overrightarrow{B_1}$ field, the T_1 and T_2 component can be ignored because the duration of

RF excitation pulse is short compared to T_1 and T_2. Equation (1.3) can be rewritten as a simpler from:

$$\frac{d\vec{M}}{dt} = \gamma\vec{M} \times \begin{bmatrix} \left|\vec{B}_1\right| \cos(\angle\vec{B}_1) \\ \left|\vec{B}_1\right| \sin(\angle\vec{B}_1) \\ B_0 \end{bmatrix}. \tag{1.4}$$

The movement of magnetization after an excitation pulse with flip angle α-pulse can be described using rotation matrix. If the initial magnetization is (0, 0, M_0)

$$\vec{M} = R_{z'}(\angle\vec{B}_1)R_{x'}(\alpha)\begin{bmatrix} 0 \\ 0 \\ M_0 \end{bmatrix} = \begin{bmatrix} M_0 \sin(\alpha)\sin(\angle\vec{B}_1) \\ M_0 \sin(\alpha)\cos(\angle\vec{B}_1) \\ M_0 \cos(\alpha) \end{bmatrix} \tag{1.5}$$

where the Rz' and Rx' are rotation operators about the z'- and x'-axis, respectively. The magnitude of $\vec{M}$ after excitation is $M_0 \sin\alpha$ and phase of the $\vec{M}$ is $\pi/2 - \angle\overrightarrow{B_1}$. Therefore, the $\overrightarrow{B_1}$ phase can be retrieved from the signal phase immediately after the RF excitation pulse.

1.2 B_1^+ mapping

The B_1^+ field produced in the object of interest has non-uniformity such as central brightening proportional to the B_0 strength due to a reduction of the RF wavelength. The study of the distribution of the transmitted RF has been performed by many study groups [6-8]. Since the accurate measurement of the $\overrightarrow{B_1}$ field is useful for many MR applications such as RF pulse designs, electric property mapping, quality control of RF coils, and correction of B_1^+ inhomogeneity in various quantitative studies [3, 9-11]. Figure 1.4 shows an example of B_1^+ magnitude and phase map distribution in a conductive phantom. These B_1^+ magnitude

maps were measured using a double angle method (DAM) and actual flip angle imaging (AFI) method [12-14].

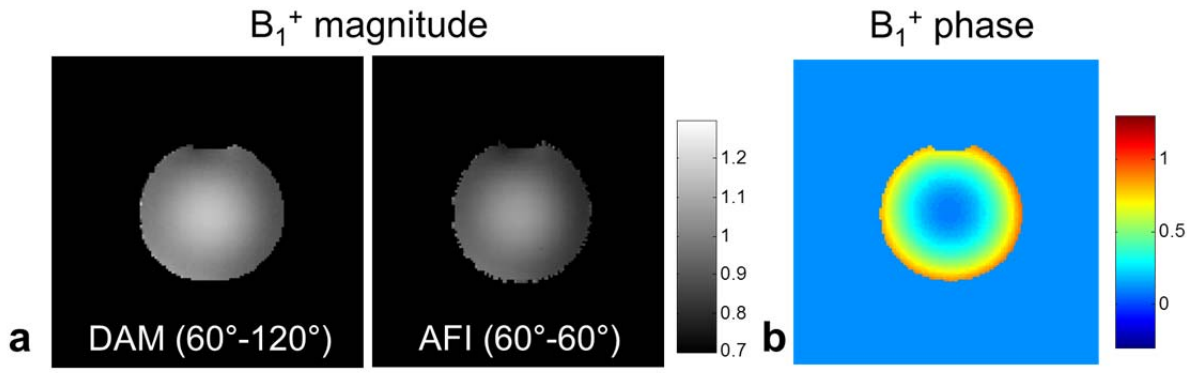

Figure 1. 4 B_1^+ magnitude (scale: [0.7 1.3]) and phase map (scale: [-0.3 1.3] rad). **a**. B_1^+ magnitude map obtained from DAM (left) and AFI (right) method. The flip angle used for each method is noted. **b**. B_1^+ phase is estimated to be half of the spin echo data acquired with DAM data.

1.2.1 B_1^+ magnitude mapping

The amplitude of the B_1^+ can be measured by several approaches [12-16]. These B_1^+ mapping methods can be divided into two types: magnitude-based and phase-based method. Magnitude-based methods use the relationship between B_1^+ and magnitude image, while phase-based methods use the relationship between B_1^+ and phase image. Each method has pros and cons in terms of scan time, accuracy, and its applications.

A simple magnitude-based method is the DAM [12, 14], which uses the signal ratios of images acquired with two different flip angles (α and 2α) to estimate the actual flip angle. The estimated flip angle (α_{DAM}) is calculated by the following equation

$$\alpha_{DAM} = \cos^{-1}\frac{S_2}{2S_1} \tag{1.7}$$

where S_1 and S_2 are the acquired images with flip angle α and 2α, respectively. The DAM method uses long TR (repetition time) to minimize the influence of the T_1 relaxation term, resulting in a long scan time. Therefore this method is not suitable for *in vivo* applications.

One commonly used 3D B_1^+ magnitude mapping method is AFI [13, 17], which measures the distribution of flip angles by acquiring data at two different TRs (TR_1 and TR_2). The estimated flip angle (α_{AFI}) is calculated by the following equation

$$\alpha_{AFI} = \cos^{-1}\frac{rn-1}{n-r} \tag{1.8}$$

where $r = S_2/S_1$ and $n = TR_2/TR_1$. S_1 and S_2 are acquired images at two different TR of TR_1 and TR_2, respectively.

Dual refocusing echo acquisition mode (DREAM) is a very fast B_1^+ magnitude mapping method [16]. This method employs a stimulated echo acquisition mode (STEAM) preparation with a single-shot gradient echo sequence and acquires the stimulated echo and FID (free induction decay) signal simultaneously. Therefore, fast estimation of the 2D B_1^+ map is possible. However, DREAM method provides a low resolution map (5 ~7 mm resolution) due to the limitation of low SNR (signal to noise ratio).

The Bloch-Siegert B_1^+ mapping method is a phase-based method which is robust to TR and T_1 relaxation effects [15]. This method provides an accurate B_1^+ magnitude map. To estimate both B_1^+ magnitude and phase, spin-echo Bloch-Siegert B_1^+ mapping method should be used. However, this method requires a relatively long TR and two separate scans to estimate B_1^+ map.

Alternatives to the above methods include using stimulated echoes [18] or the signal nulling method [19]. Multiple TR B_1/T_1 mapping (MTM) [20], phase-sensitive method of flip angle mapping [21], or $\overrightarrow{B_1}$ estimation using adiabatic refocusing (BEAR) [22] are recently proposed as a progressive method.

1.2.2 B_1^+ phase mapping

Together with the B_1^+ magnitude map, B_1^+ phase also holds valuable information for applications such as RF transmit/receive characterization [23, 24] and electric property mapping, which require both B_1^+ magnitude and phase information [3, 25, 26].

Ideally, MR signal at TE (echo time) =0 contains contributions from the B_1^+ and B_1^- phases; however, not all of this information can be acquired. The B_1^+ is related to the RF transmitter while B_1^- is related to the RF receiver [27]. Conventional spin echo (SE) sequences can be used to deduce the TE=0 phase information while removing the effects of B_0 inhomogeneity. Using a parallel transmit coil, B_1^+ phase could be used to separate from the MR signal [28]. However, using a single transmit coil, separation of the B_1^+ phase is difficult. For certain coil arrangements or object geometries , the B_1^+ phase is approximately the same as the B_1^- phase. Therefore, the B_1^+ phase can be estimated as half of the TE=0 phase (i.e., half the SE phase or balanced steady-state free precession (bSSFP) phase) [1, 26, 27]. Figure 1.5 shows the simulation results of the RF transmit and receive phase. The head model has a bilateral symmetry and the above assumption that $\angle B_1^+ \fallingdotseq \angle B_1^-$ can be applied. Simulation results show similar distributions of B_1^+ phase (figure 1.5b) and B_1^- phase (figure 1.5c).

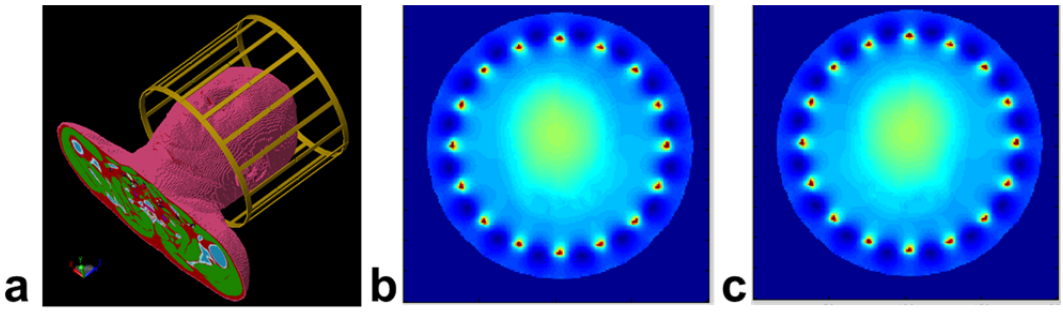

Figure 1. 5 Simulation results of the RF transmit and receive phase. **a.** Phantom model. **b.** B_1^+ phase of the RF transmit field. **c.** B_1^- phase of the RF receive field.

1.3 Electrical property mapping

This dissertation deals with the electrical properties of tissues such as conductivity, permittivity and loss tangent. The electrical properties of tissues have been measured using sensors or probes in many dosimetry studies [29-31]. The dielectric properties of biological tissues can be used in various fields, for example, to explain the molecular processes, to measure the specific absorption rate (SAR) [2], and to simulate the electromagnetic field inside the human body with the wireless telecommunication environment. Moreover, the information of electrical properties of human body provides diagnosis and treatment of various oncologic diseases, radio-frequency hyperthermia, electrocardiography, and functional and structural information of human body [32-35].

1.3.1. Frequency dependent dielectric properties

The dielectric properties of a biological tissue are determined from the interaction of electromagnetic field with tissue at the cellular level. These properties vary with the frequency of the electromagnetic field. Typically, soft tissues exhibit a continuous decrease in permittivity with frequency increase while the conductivity increases with frequency increase. The dependency on frequency can be divided into three regions dependent on the dominant physical mechanism and is commonly referred as α, β and γ dispersions. The origin of conductivity in the α dispersion, in the low frequency region which is below few kHz, is associated with ionic diffusion processes at the site of the cellular membrane. In the β dispersion which is in the hundreds of kilohertz region, the conductivity variation is dominated by the polarization of cellular membranes and the polarization of protein and other organic macromolecules. The variation of the conductivity in the γ dispersion, in the gigahertz region, is due to the polarization of water molecules [36].

MREPT (magnetic resonance electric properties tomography) and MREIT (magnetic resonance electrical impedance tomography) are mainly used techniques to measure the electrical properties. These two methods provide the electrical conductivity of biological tissues at different frequencies. MREIT provides low-frequency (below 1kHz) conductivity [37]. This technique estimates the contrast information of conductivity by injecting low frequency current to an object. MREIT gives information of cellular structure since low frequency currents can's pass through the inside of cells [38]. MREPT is a recently introduced technique which is a non-invasive estimation method of probing electrical properties [2, 26, 39]. MREPT provides high-frequency (at the Larmor frequency, 64-300 MHz with 1.5-7T MRI) conductivity using the B_1^+ map [2]. At high frequencies, the conductivity is not affected by the membrane since the high frequency current can penetrate everywhere regardless of the membrane. MREPT data enable the quantitative analysis of absolute conductivity [40].

1.3.2 Relation between electrical property and RF propagation

The magnetic field inside the MR system varies for each patient. Also, RF field distribution inside the patient is affected by the geometry and electromagnetic properties of the human body. From time-harmonic Maxwell equations,

$$\nabla \times \vec{E} = -i\omega\mu_0 \vec{H} \tag{1.9}$$

$$\nabla \times \vec{H} = (\sigma + i\omega\varepsilon)\vec{E} \tag{1.10}$$

where $\vec{E}$ is the electric field, $\vec{H}$ is the magnetic field, μ_0 is a permeability in vacuum, σ is the conductivity, ω is the angular frequency, and ε is the permittivity. Taking the curl to equation (1.10)

$$\nabla \times \nabla \times \vec{H} = \nabla \times (\sigma + i\omega\varepsilon)\vec{E} = \nabla(\sigma + i\omega\varepsilon) \times \vec{E} - (\sigma + i\omega\varepsilon)\nabla \times \vec{E}\,. \tag{1.11}$$

Since the $\nabla\times\nabla\times\vec{H}$ can be rewritten as -$\nabla^2\vec{H}$, equation (1.11) is represented following equation

$$-\nabla^2\vec{H}=\frac{\nabla(\sigma+i\omega\varepsilon)}{\sigma+i\omega\varepsilon}\times(\nabla\times\vec{H})-i\omega\mu_0(\sigma+i\omega\varepsilon)\vec{H}\,. \tag{1.12}$$

From this relation between electrical properties and magnetic field, the electrical conductivity and permittivity of tissues can be acquired by measuring B_1^+ map ($\overrightarrow{B_1}=\mu_0\vec{H}$).

1.3.3 Magnetic resonance electric properties tomography (MREPT)

Most MREPT reconstruction algorithms assume homogeneous electrical properties inside each tissue. With this assumption, the first term of the right side of the equation (1.12) can be ignored and then the equation (1.12) becomes a Helmholtz equation

$$\nabla^2\vec{H}-i\omega\mu_0(\sigma+i\omega\varepsilon)\vec{H}=0\,. \tag{1.13}$$

The RF magnetic field of the MR system is circularly polarized so that the notation $H^+ = (H_x+iH_y)/2$ is convenient to use instead of $\vec{H}$. Since each component of $\vec{H}$ satisfies the equation (1.13), H^+ also satisfies

$$\nabla^2H^+-i\omega\mu_0(\sigma+i\omega\varepsilon)H^+=0\,. \tag{1.14}$$

Electrical properties are directly solved by equation (1.14), the H^+ can be replaced with B_1^+

$$\sigma(r)+i\omega\varepsilon(r)=\frac{\nabla^2H^+(r)}{i\omega\mu_0H^+(r)}=\frac{\nabla^2B_1^+(r)}{i\omega\mu_0B_1^+(r)}\,. \tag{1.15}$$

Equation (1.15) is correct over homogeneous phantom or tissues. Due to the assumption of $\nabla(\sigma+i\omega\varepsilon)=0$, estimation error occurs at the boundary of tissues and inhomogeneous regions. In addition, this algorithm is sensitive to fluctuation of signal and noise due to the Laplacian operator. These effects can be reduced to apply smoothing filters.

1.4 Motivation

The main motivation to develop and use electrical property mapping is because it can give complement information to conventional images and generate a new contrast image which can help medical diagnosis. Although the electrical properties of biological tissues have been used in various fields, most of the studies measured the *ex vivo* electrical properties or were performed on animals, due to the limitation of invasive measurement.

MREPT uses B_1^+ map to solve the Helmholtz equation and determine the electrical properties. Accurate B_1^+ map is necessary to determine the electrical property. The B_1^+ phase did not gain much interest to the MRI community previous to the appearance of MREPT, B_1^+ phase mapping method is hard to find contrary of the plenty of B_1^+ magnitude mapping method. Especially for conductivity mapping, B_1^+ phase should have high SNR as B_1^+ magnitude.

Moving spins such as blood flow disturbs B_1^+ phase mapping because motion itself generates phase modulation in MRI. The phase perturbation from the flow generates severe estimation error of conductivity. The conductivity variation by the flow is observed many study groups [32, 41]. Therefore, the flow effect should be taken into consideration when measuring B_1^+ phase. Since the flow effect is hard to remove using a conventional method, there is a need to develop a flow compensated B_1^+ mapping method.

1.5 Outline of this dissertation

In chapter 2, a simultaneous B_1^+ magnitude and phase mapping is suggested. To acquire the B_1^+ magnitude and phase simultaneously, a modified multi-echo AFI sequence is proposed. A multi-echo gradient echo sequence was integrated into every even TR of AFI to measure both magnitude and phase of B_1^+. To increase the signal-to-noise ratio of the B_1^+ phase, a double-angle multi-echo AFI sequence, in which the flip-angle of the RF pulses is α at the odd TR and 2α at the even TR is proposed. Images were simulated to evaluate the performance of this method by adjusting various imaging and physical parameters. The performance was compared to the spin echo based B_1^+ mapping method in both phantom and *in vivo* studies.

The purpose of chapter 3 is to visualize the dielectric loss tangent of tissue using MRI and observe the effect of loss tangent in the process of hyperthermia from simulations. The non-invasive loss tangent imaging method was proposed at the Larmor frequency. Electromagnetic simulations of hyperthermia were performed to observe temperature elevation, energy efficiency, and penetration depth with respect to loss tangent using the Bessel boundary matching method. For measurement of tissue loss tangent, radio frequency field maps (B_1^+ map) were acquired using a double-angle AFI sequence. The conductivity and permittivity were obtained from the complex B_1^+ map using Helmholtz equation. Phantom and *ex vivo* experiments were performed for verification.

Chapter 4 focused on the reconstruction of *in vivo* conductivity map using flow compensated double spin echo signals and analysis of flow induced effects in B_1^+ phase to improve the estimation of electrical conductivity. The estimation of flow conductivity was also pursued in this work. To remove additional phase, spatial polynomial fitting was applied

using information of velocity encoded phase acquired from a separate acquisition. Phantom and *in vivo* experiments were performed to validate proposed method.

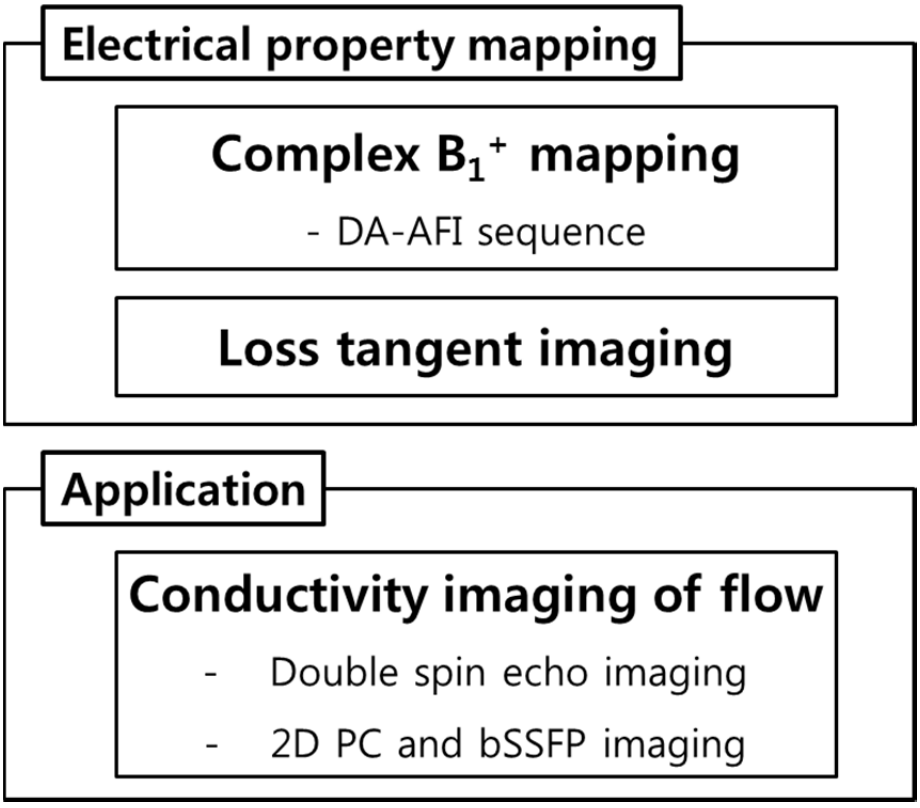

Figure 1. 6 Outline of the dissertation. In the chapter 2, the complex B_1^+ mapping method is suggested. Chapter 3 analyzes and visualizes the loss tangent. Chapter 4 focuses on the reconstruction of *in vivo* conductivity map.

Chapter 2

A modified multi-echo AFI for simultaneous B_1^+ magnitude and phase mapping

2.1 Introduction

Measurement of transmit RF field, which is called B_1^+ mapping, can be useful for many MR applications such as determining local RF power [42, 43], measuring RF coil performance [11, 44], mitigating B_1^+ inhomogeneity using a parallel transmit system [6, 7], correcting B_1^+ inhomogeneity effects in various quantitative studies [9, 10, 45, 46], and mapping electric property constants [2, 3, 26, 47, 48].

Several approaches have been developed to map B_1^+ magnitude [12-16, 22]. Each method uses a relationship between B_1^+ and acquired signal to measure B_1^+ magnitude. These methods have limitations such as long scan time, low SNR, or multiple numbers of scan.

AFI, which introduced in chapter 1.2.1, measures the distribution of flip angles by acquiring data at two different TRs. Assuming the transverse magnetization is completely spoiled and repetition times are much shorter than the longitudinal relaxation time ($TR_1 < TR_2 << T_1$), the flip angle (α) can be estimated from two different images (S_1 and S_2) measured at TR_1 and TR_2, respectively [17].

While most applications use a measured B_1^+ magnitude map, the B_1^+ phase also holds valuable information for many applications which are specified in chapter 1.2.2. Especially, to calculate electrical conductivity, accurate B_1^+ phase measurements are necessary together with the precise B_1^+ magnitude mapping [3, 25].

The absolute B_1^+ phase is difficult to obtain, therefor, current method have difficulty in measuring it. Information of TE=0 phase can be used to measure B_1^+ phase. Conventional SE and bSSFP sequences can be used to deduce the TE=0 phase information while removing the effects of B_0 inhomogeneity. However, simultaneous mapping of B_1^+ magnitude and phase from spin echo pulse sequence requires long scan times to acquire 3D images.

To obtain B_1^+ magnitude and phase simultaneously, a multi-echo AFI sequence is proposed that integrates an AFI sequence with a multi-echo gradient echo sequence to estimate the B_1^+ phase [8, 49]. AFI sequence is modified to a double-angle multi-echo AFI (DA-AFI) sequence where the flip angle for the multi-echo gradient portion is doubled to increase the signal-to-noise ratio (SNR) in the mapping of B_1^+. Numerical simulations were performed to observe performances of the proposed sequence and determine the optimal flip angles and the number of echoes. DA-AFI can provide 3D whole-body B_1^+ magnitude and phase with a fast single-scan procedure. Comparison with conventional AFI, this approach has small noise standard deviation at both B_1^+ magnitude and phase without additional scan time. Phantom and *in vivo* imaging experiments were performed for the validation of proposed method.

2.2 Methods

2.2.1 Double flip-angle AFI

A multi-echo gradient echo sequence was combined with AFI using two different flip angles to acquire the complex B_1^+ map, which includes both magnitude and phase. The sequence diagram is described in figure 2.1. The initial gradient echoes (S_1, S_2) were acquired at both TRs (TR_1, TR_2) to calculate B_1^+ magnitude ($\hat{B}_{1mag}$). Echoes acquired at TR_2 (S_2, S_3, …) were used to calculate B_1^+ phase ($\hat{B}_{1phase}$). While precision of $\hat{B}_{1mag}$ is determined by

both S_1 and S_2, The signal intensities acquired at TR_2 determines the precision of $\hat{B}_{1phase}$. In the original AFI sequence, the signal intensity at TR_2 was usually lower than that at TR_1, since longitude magnetization may be less recovered to a steady state if $TR_1 < TR_2 << T_1$. To obtain high signal intensity at TR_2, the flip angles were adjusted such that TR_2 has twice the flip angle of TR_1 (first flip angle, α; second flip angle, 2α). Thus, using a similar approach to [17], the flip angle can be reconstructed by the following closed-form equation.

$$\alpha \approx \cos^{-1}\left(\frac{1-\sqrt{1-2(r-n)r(n-1)}}{2(n-r)}\right),\ where\ r=\frac{S_2}{S_1},\ n=\frac{TR_2}{TR_1} \tag{2.1}$$

The details of the derivation are followed. In steady-state, the longitudinal magnetizations for TR_1 and TR_2 before excitation are

$$M_{z1}=M_0\frac{1-E_2+(1-E_1)E_2\cos\alpha_2}{1-E_1E_2\cos\alpha_1\cos\alpha_2} \tag{2.2}$$

$$M_{z2}=M_0\frac{1-E_1+(1-E_2)E_1\cos\alpha_1}{1-E_1E_2\cos\alpha_1\cos\alpha_2} \tag{2.3}$$

where $E_{1,2}=\exp(-\frac{TR_{1,2}}{T_1})$ and M_0 represents equilibrium magnetization. The acquired signals S_1 and S_2 can be expressed as:

$$S_{1,2}=M_{z1,2}\exp(-\frac{TE}{T_2^*})\sin\alpha_{1,2}\,. \tag{2.4}$$

The ratio *r* of the magnitudes of the two images is formed giving

$$r=\frac{S_2}{S_1}=\left(\frac{1-E_1+(1-E_2)E_1\cos\alpha_1}{1-E_2+(1-E_1)E_2\cos\alpha_2}\right)2\cos\alpha_1 \tag{2.5}$$

with the condition that the second flip angle is twice the first flip angle ($\alpha_2 = 2*\alpha_1$). For short TR_1 and TR_2, a first-order approximation is applied to simplify Eq. (2.5).

$$r\cong\left(\frac{1+n\cos\alpha_1}{n+2\cos^2\alpha_1-1}\right)2\cos\alpha_1 \tag{2.6}$$

where $n = \frac{TR_2}{TR_1}$. After solving a quadratic equation for α_1, the flip angle α_1 is estimated as

$$\alpha_1 \approx \cos^{-1}\left(\frac{1 \pm \sqrt{1-2(r-n)r(n-1)}}{2(r-n)}\right). \tag{2.7}$$

Generally, *n* is larger than two, which makes the term in the root larger than or equal to zero. If the flip angle is in the range from 0° to 90°, the sign in front of the root is negative. Hence, the α is derived as

$$\alpha_1 \approx \cos^{-1}\left(\frac{1 - \sqrt{1-2(r-n)r(n-1)}}{2(r-n)}\right). \tag{2.1}$$

An assumption that TR_1 and TR_2 are much shorter than the T_1 relaxation time was used similar to AFI, therefore, the accuracy of the approximated equation (2.1) is changed under varying TR and relaxation conditions.

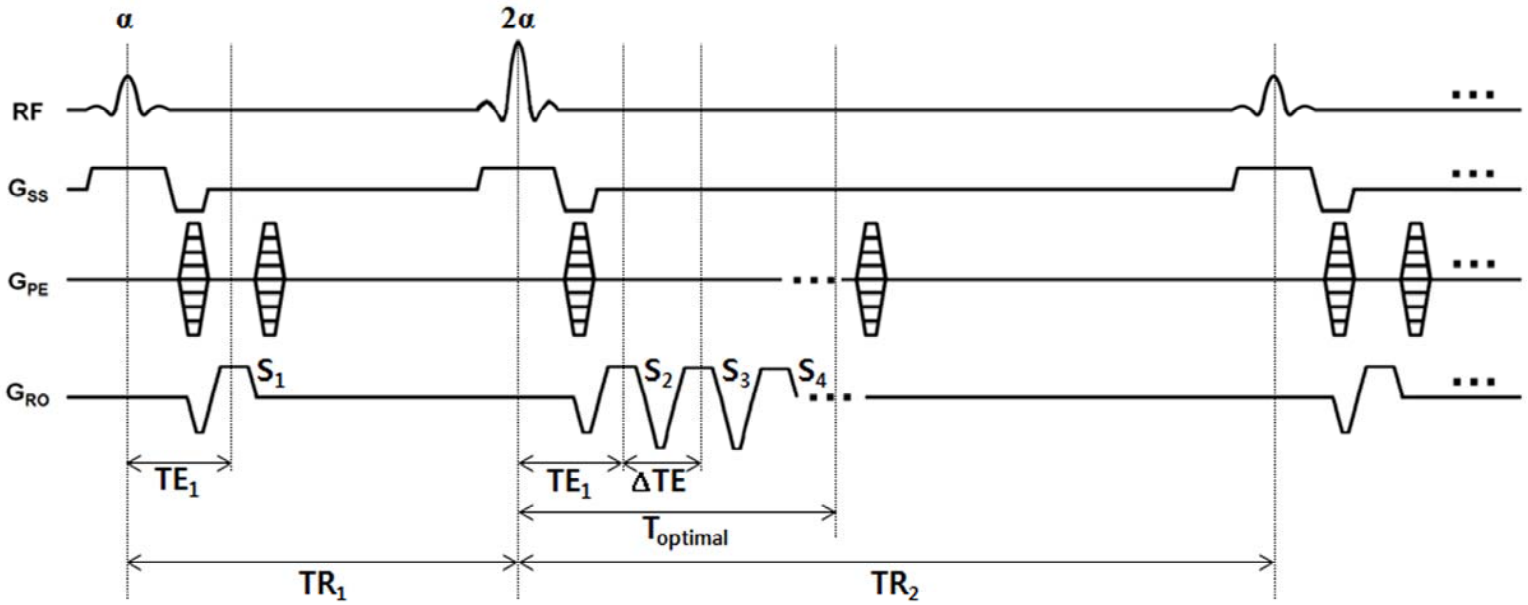

Figure 2. 1 Pulse sequence diagram of double-angle multi-echo AFI. The RF flip angle of the second pulse was twice the RF flip angle of the first pulse. Multi-echo gradient echoes were acquired during the second pulse. Spoiling gradients were applied on each of the three gradient axes (not shown). The total spoiling gradient area at TR_2 was n ($=TR_2/TR_1$) times the gradient area at TR_1.

The signal intensities S_1, S_2 were calculated based on equations (2.2), (2.3), and (2.4) and intrinsic estimation error in the flip angle estimate was computed using equation (2.1). Figure 2.2 illustrates the estimation errors with the variation of TR, T_1 relaxation time and the TR ratio (*n*). Simulations in (a) were performed with TR_1/T_1 ratios of 0.02, 0.06, and 0.2 and *n*=5 (e.g., TR_2/TR_1: 150/30ms). These values were chosen with actual T_1 values in mind (1500, 500, and 150ms). The simulations in (b) were performed with values of n=2, 3, 5, 10, and 15 at TR_1/T_1=0.06 (e.g., TR_1: 30ms, T_1: 500ms). Flip-angle estimates become worse at low flip angles due to noise corruption. The estimation error was less than 8% even TR_1/T_1: 0.5 and *n*: 5 (figure 2.2a), suggesting that the first-order approximation in equation (2.5) holds for a broad range of T_1. The TR ratio, *n*, also affects the performance of B_1^+ magnitude mapping (figure 2.2b), which is related to the dynamic range of flip-angle variations. Estimation errors less than 5% were achieved as long as *n* was greater than 3. Increasing *n* makes the variation in the signal ratio with respect to the flip angle almost linear and also reduces the intrinsic error of equation (2.1). Due to the trade-off in the scan time, the recommended *n* is in the range of 5-6. Hence, in this implementation, TR_1:TR_2 was set at 30ms:150ms, corresponding to *n*=5.

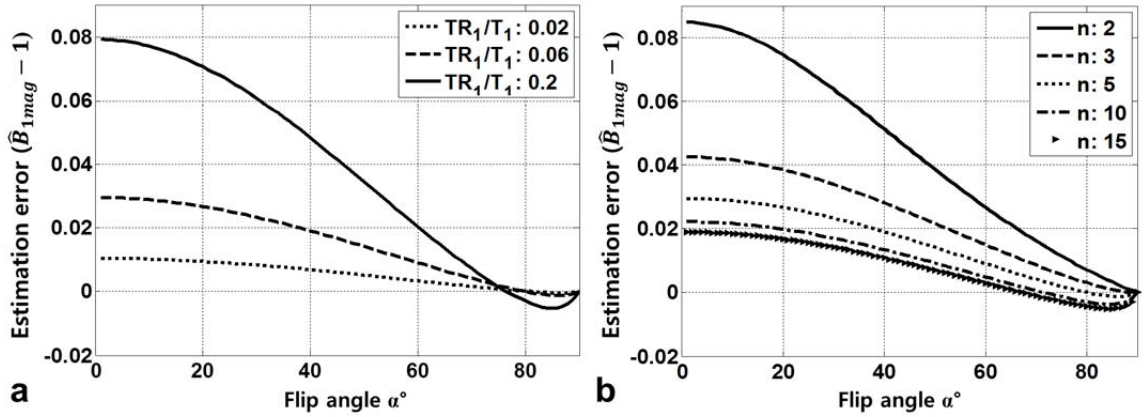

Figure 2. 2 Simulations of the flip angle estimation error ($\hat{B}_{1mag}$ -1) for the double-angle multi-echo AFI as a function of the flip angle. **a:** Effect of varying TR_1/T_1 ratio. The simulations were performed with varying TR_1/T_1 (0.02, 0.06, and 0.2) at n=5 (e.g., TR_2/TR_1: 150/30ms). **b:** Effect of varying n. The simulations were performed with varying n (2, 3, 5, 10, and 15) at TR_1/T_1: 0.06 (e.g., TR_1: 30ms, T_1: 500ms).

2.2.2 Estimation of phase at TE = 0 using multi-echo gradient echo

In gradient echo based sequence, the phase can be regarded as a sum of the phase produced by RF pulse penetration (φ_0) and a linear accumulation due to B_0 inhomogeneity:

$$\varphi(x,y,z) \cong \varphi_0(x,y,z) - \gamma \Delta B_0 t \tag{2.8}$$

To determine φ_0 (the initial phase at TE=0 produced by the RF transmit and receive process), a multi-echo gradient echo sequence was used to remove the effect of B_0 inhomogeneity. From images acquired at multiple TEs, the phase for each pixel can be fitted by most simply using a first-order linear least-squares fitting. The phase mapping equation can be written as:

$$\begin{bmatrix} -\gamma \Delta B_0 \\ \varphi_0 \end{bmatrix} = \begin{bmatrix} TE_1 & 1 \\ TE_2 & 1 \\ \vdots & \vdots \\ TE_N & 1 \end{bmatrix}^{+} \begin{bmatrix} \varphi_1 \\ \varphi_2 \\ \vdots \\ \varphi_N \end{bmatrix} + \begin{bmatrix} TE_1 & 1 \\ TE_2 & 1 \\ \vdots & \vdots \\ TE_N & 1 \end{bmatrix}^{+} \begin{bmatrix} n_{\varphi_1} \\ n_{\varphi_2} \\ \vdots \\ n_{\varphi_N} \end{bmatrix}, \; TE_i = TE_1 + (i-1) \cdot \Delta TE \; where \; i \geq 2 . \tag{2.9}$$

where φ_i represents the phase at TE_i, $^+$ represents a pseudo-inverse of the matrix, and $n_{\varphi i}$ represents a Gaussian distributed noise term for echo i. In bilateral symmetry case, such as a head in a bird cage coil, the B_1^+ phase is half of the transceive phase ($\angle B_1^+ \approx \varphi_0/2$) [1, 26, 27].

A 4D phase unwrapping process was performed using the PRELUDE phase unwrapping method [50]. A global phase was removed after the initial phase estimation.

2.2.3 Intrinsic error of the B_1^+ mapping

Using values from the above simulations (i.e., n=5), the mapping error was calculated from both AFI and DA-AFI. By the law of error propagation, the error in $\hat{B}_{1mag}$ can be calculated as follows:

$$\sigma^2_{\hat{B}_{1mag}} = \left(\frac{\partial f}{\partial S_1}\sigma_1\right)^2 + \left(\frac{\partial f}{\partial S_2}\sigma_2\right)^2 \tag{2.10}$$

where the $\sigma_{\hat{B}_{1mag}}$ is the standard deviation of error in the $\hat{B}_{1mag}$, function f is the B_1^+ magnitude mapping equation given by AFI and DA-AFI (equation (2.1)), respectively, and $\sigma_{1,2}$ is the standard deviation of noise in the signal $S_{1,2}$.

For B_1^+ phase mapping, from second term on the right-hand side of equation (2.9), the noise can be expressed as

$$\begin{bmatrix} TE_1 & 1 \\ TE_2 & 1 \\ \vdots & \vdots \\ TE_N & 1 \end{bmatrix}^+ \begin{bmatrix} n_{\varphi_1} \\ n_{\varphi_2} \\ \vdots \\ n_{\varphi_N} \end{bmatrix} = \begin{bmatrix} c_1 n_{\varphi_1} + c_2 n_{\varphi_2} + \cdots + c_N n_{\varphi_N} \\ d_1 n_{\varphi_1} + d_2 n_{\varphi_2} + \cdots + d_N n_{\varphi_N} \end{bmatrix}. \tag{2.11}$$

The coefficients c_i and d_i (i=1, 2, …, N) are elements of the pseudo-inverse matrix. The error standard deviation in the $\hat{B}_{1phase}$ can be calculated as

$$\sigma^2_{\hat{B}_{1\,phase}} = (d_1\sigma_1)^2 + (d_2\sigma_2)^2 + \cdots + (d_N\sigma_N)^2 \quad (2.12)$$

where $\sigma_{\hat{B}_{1\,phase}}$ is the standard deviation of error in the $\hat{B}_{1\,phase}$, σ_i denotes the standard deviation for noise in the phase. The intrinsic errors, defined in equation (2.10) and equation (2.12), were compared between the proposed DA-AFI and the original AFI. Steady-state signals (S_1, S_2) were produced for these two methods based on equations (2.2), (2.3), and (2.4). T_2^* relaxation was concerned to produce multi-echo signals (S_3, S_4, …).

2.2.4 Optimal echo number selection

To determine the number of echoes for the estimation of φ_0, Monte Carlo simulations were performed having various T_2* values. Three sets of phase data using multi-echo gradient echo were generated at 20, 55, and 75ms of T_2* relaxation times based on the reported T_2* values of liver, white matter, and gray matter at 3T [51, 52]. The SNR of the first echo set to 50 by adding Gaussian noise into the complex data. More than 50,000 iterations were performed to guarantee precision of the simulation. The first TE was assumed to be 3.55ms, and the echo spacing was 3.55ms. In addition, three sets of data were produced with 10, 50, and 200 SNRs of the first echo. The $\sigma_{\hat{B}_{1\,phase}}$ were observed with respect to the number of fitted echoes with various T_2* relaxation times. The last TE value, which is equal to the time required for the fitted echoes to get minimum noise standard deviation, was defined as $T_{optimal}$ (figure 2.1). The $T_{optimal}$ values were fitted to a first-order function.

Figure 2.3a shows the noise standard deviation of the estimated φ_0 ($\sigma_{\hat{B}_{1\,phase}}$) calculated by equation (2.12). The number of echoes which provides the most robust phase estimation was 7, 18, and 23 for T_2* values of 20, 55 and 75ms, respectively ($T_{optimal}$: 24.85, 63.9, and 81.65ms). The $T_{optimal}$ time had a linear correlation with the tissue T_2* value regardless of

SNR (figure 2.3b). The slope and coefficient of determination (R^2) of each linear fit graph are noted. Hence, echoes were used to estimating TE=0 phase until 60% signal decay.

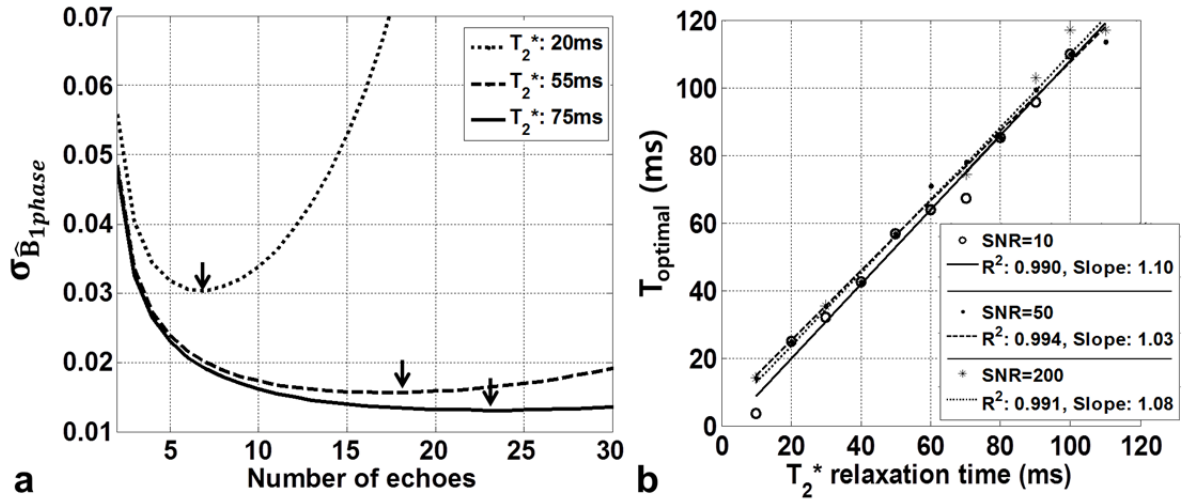

Figure 2. 3 Simulation results to determine optimal number of echoes. **a:** $\sigma_{\hat{B}_{1\,phase}}$ with respect to the number of fitted echoes. Actual T_2* values were 20, 55, and 75ms (SNR: 50). The numbers of echoes with minimum errors are marked with arrows. **b:** $T_{optimal}$ values are marked with dots (SNR: 10, 50, 200). The fitted lines show the linear correlation between $T_{optimal}$ and tissue T_2* values with high R^2 values regardless of SNR.

2.2.5 Experiments

For the performance estimation of the proposed method, axial images of a cylindrical phantom were obtained from 3.0T MRI scanner (Tim Trio, Siemens Medical Solutions, Erlangen, Germany) using a transceive quadrature head coil. Sixteen slices were acquired in 3D mode with resolution of 2.0 × 2.0 × 4.0 mm^3 voxel size. The parameters of the DA-AFI sequence were TR_1/TR_2= 30/150ms (n=5), $\alpha_{1,2}$= 40°-80°, first TE= 3.35ms, echo spacing= 3.55ms, FOV= 128×256 mm^2, number of echoes= 6, leading to scan time of 3 minutes 42 seconds. To compare the multi-echo AFI methods, same parameters were used except $\alpha_{1,2}$: 60°-60°. A standard reference B_1 map was obtained from the SE data set using the DAM

technique [12]. The data set was obtained from 2D multi-slice mode with the following parameters: TR/TE= 2000/12ms; α= 60° and 120°, resolution of 2.0×2.0×4.0 mm^3 voxel size and total scan time was 4 minutes 40 seconds.

To image *in vivo* brain, a healthy normal volunteer was scanned with the 3D DA-AFI sequence and the multi-echo AFI sequence using the quadrature head coil. Written consent was obtained from the volunteer. Sixteen slices were obtained with 2.0 × 2.0 × 4.0 mm^3 resolution, TR_1/TR_2= 40/200ms, first echo time= 3.55ms, echo spacing= 3.55ms, $\alpha_{1,2}$= 40°-80°, FOV= 256×256 mm^2, leading to a total scan time of 8 minutes 12 seconds.

2.3 Results

2.3.1 Numerical simulation

The noise standard deviations of the original AFI method (α-α) and the proposed DA-AFI method (α-2α) were calculated by the equations (2.10) and (2.12), and were described in figure 2.4. A reciprocal number of the noise standard deviation was analyzed to emphasize its high-performance ranges. The calculated $1/\sigma_{\hat{B}_{1mag}}$ and $1/\sigma_{\hat{B}_{1phase}}$ for AFI and DA-AFI (n=5) show the mapping accuracy of each method. Compare to multi-echo AFI, B_1^+ mapping performance was improved by adjusting the flip angle keeping the same scan time. Contour lines (figure 2.4b-c) illustrate the outperformed range for B_1^+ mapping which has positive differences between DA-AFI and AFI at different TR_1/T_1 and n. Accurate magnitude mapping using high flip angles is beneficial, especially over 50°, where DA-AFI was always more accurate than the AFI method regardless of TR_1/T_1. The B_1^+ phase mapping accuracy has the advantage of using low flip angles (e.g., less than 40°) since the steady-state signal intensity is magnificently decreased at high flip angles with short TR. In the overlapped

region (shaded in Figs. 4b-c), DA-AFI outperformed AFI for both magnitude and phase mapping. Parameters (e.g., scan time, B_1^+ magnitude map accuracy, and etc.) can be adjusted to the purpose of the experiment.

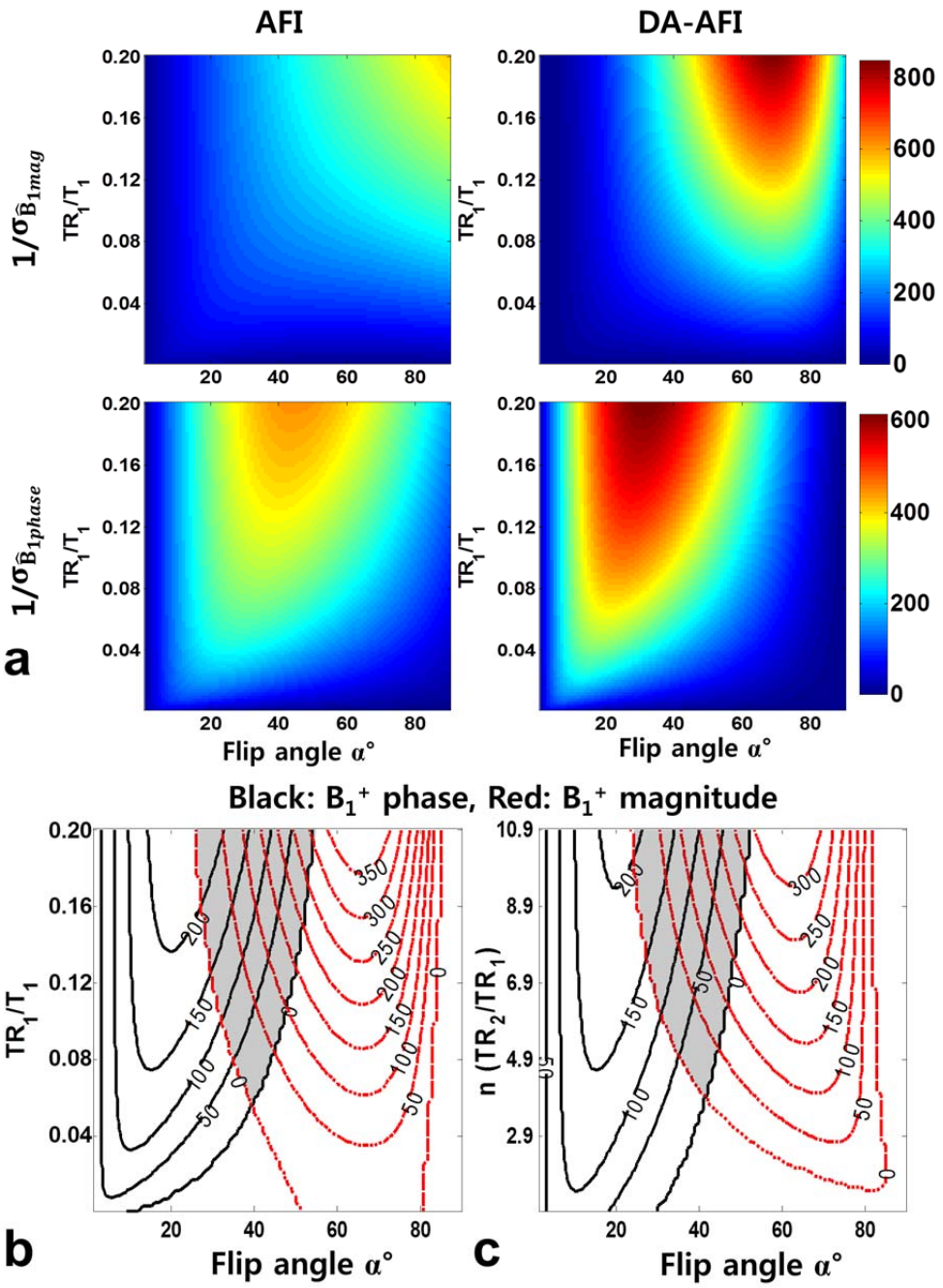

Figure 2. 4 Performance evaluation of multi-echo AFI and double-angle multi-echo AFI sequence. **a:** $1/\sigma_{\hat{B}_{1mag}}$ and $1/\sigma_{\hat{B}_{1phase}}$ for AFI and DA-AFI. **b,c:** Difference of the $1/\sigma$ between DA-AFI and AFI. Contour lines illustrate the outperformed range which has positive differences between DA-AFI and AFI (b: n=5, c: TR_1/T_1=0.08) for B_1^+ mapping. The numbers on each line indicate differences between DA-AFI and AFI. Each shaded area represents the preferred parameters for B_1^+ complex mapping using DA-AFI.

2.3.2 Phantom experiment

Figure 2.5 shows the phantom images obtained from both AFI and DA-AFI sequences. The S_1 and S_2 images represent varying signal intensity according to the flip angle (figure 2.5a-b). The S_2 images show high SNR with flip angle of 40° to 80°. The estimated complex B_1^+ map is shown in figure 2.5c-d. The left and right map is estimated from AFI and DA-AFI, respectively. Patterns of the estimated B_1^+ magnitude using three different methods were highly correlated (figure 2.5c, e). Compared to DAM, the B_1^+ magnitude was underestimated by 8.73% in AFI while overestimated by 7.59% in DA-AFI across the entire FOV. These bias errors originate from the use of first-order approximation. The calculated average $1/\sigma_{\hat{B}_{1mag}}$ values by equation (2.10) were 521.91 for 60°-60° (AFI) and 527.41 for 40°-80° (DA-AFI). The proposed DA-AFI method (dashed line) shows less noise than the AFI method (solid line) in the $\hat{B}_{1mag}$. Figures 2.5d and 2.5f depict $\hat{B}_{1phase}$ and line profiles of the center lines, respectively. Estimated B_1^+ phase maps are highly correlated. Noise standard deviations were calculated by equation (2.12) to compare the noise in each phase image. The calculated $\sigma_{\hat{B}_{1phase}}$ values were 0.0032 for AFI and 0.0025 for DA-AFI. These values were normalized to 1.28 and 1 for convenience. The proposed DA-AFI method shows less statistical error than common AFI in the B_1^+ phase map. Figure 2.5g represents the TE=0 phase and SE phase. The correlation coefficient between TE=0 phase and SE phase was 0.9890.

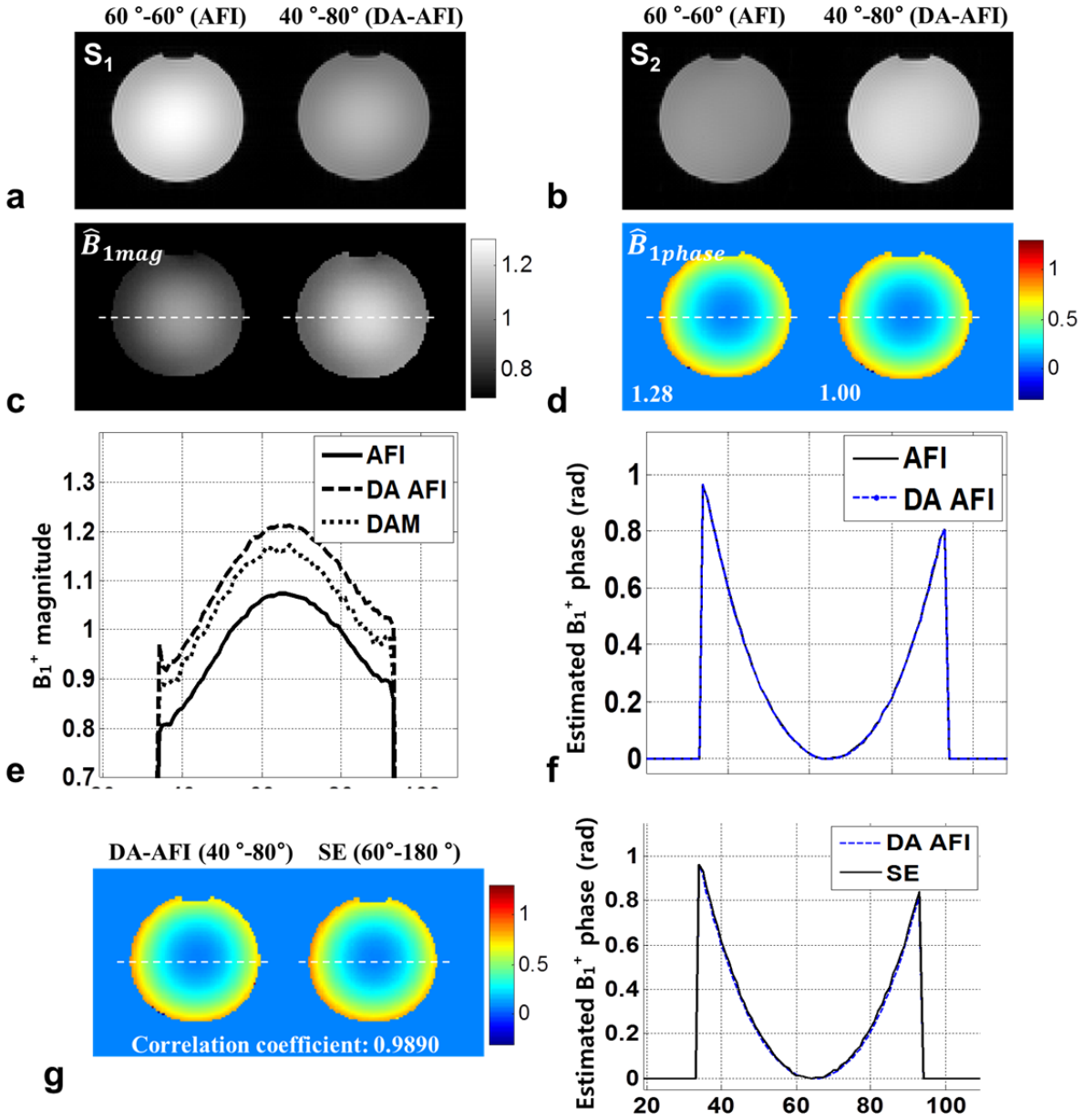

Figure 2. 5 Results of the phantom experiment. **a, b:** Images obtained from AFI and DA-AFI. S_1 is obtained at TR_1 and S_2 is obtained at TR_2. **c, d:** B_1^+ magnitude (scale: [0.7 1.3]) and phase map (scale: [-0.3 1.3] rad). The left and right map is estimated from AFI and DA-AFI, respectively. The normalized noise standard deviation of the phase is written on each figure (d). **e, f:** Line profiles (white lines on (c) and (d)) of the magnitude and phase, respectively. The dotted line in (e) is a line profile of the DAM that is inserted to compare the performance of B_1^+ magnitude mapping. **g:** TE=0 phase and SE phase and its line profiles. The correlation coefficient between TE=0 phase and SE phase is written on the figure.

2.3.3 Human experiment

Figure 2.6 demonstrates *in vivo* brain B_1^+ mapping using 3D DA-AFI. The anatomical information is clearly shown in S_1 images (figure 2.6a). These image magnitudes show stable performance at three different slices. Figure 2.6b shows small variation of signal intensity in the B_1^+ magnitude. The $\hat{B}_{1mag}$ map varies from -10% to 20% relative to the nominal flip angle through the entire FOV. The enhanced B_1^+ signal in the ventricular region originates from the relaxation effects and conductivity contrast. The $\hat{B}_{1phase}$ maps show similar patterns except in the vessels which are illustrated in figure 2.6c. Although the B_0 effect was tried to eliminate, accurate phase measurement at certain areas such as air-tissue interfaces was limited by signal loss due to strong B_0 inhomogeneity in that areas with the mixture of linear and non-linear inhomogeneity components.

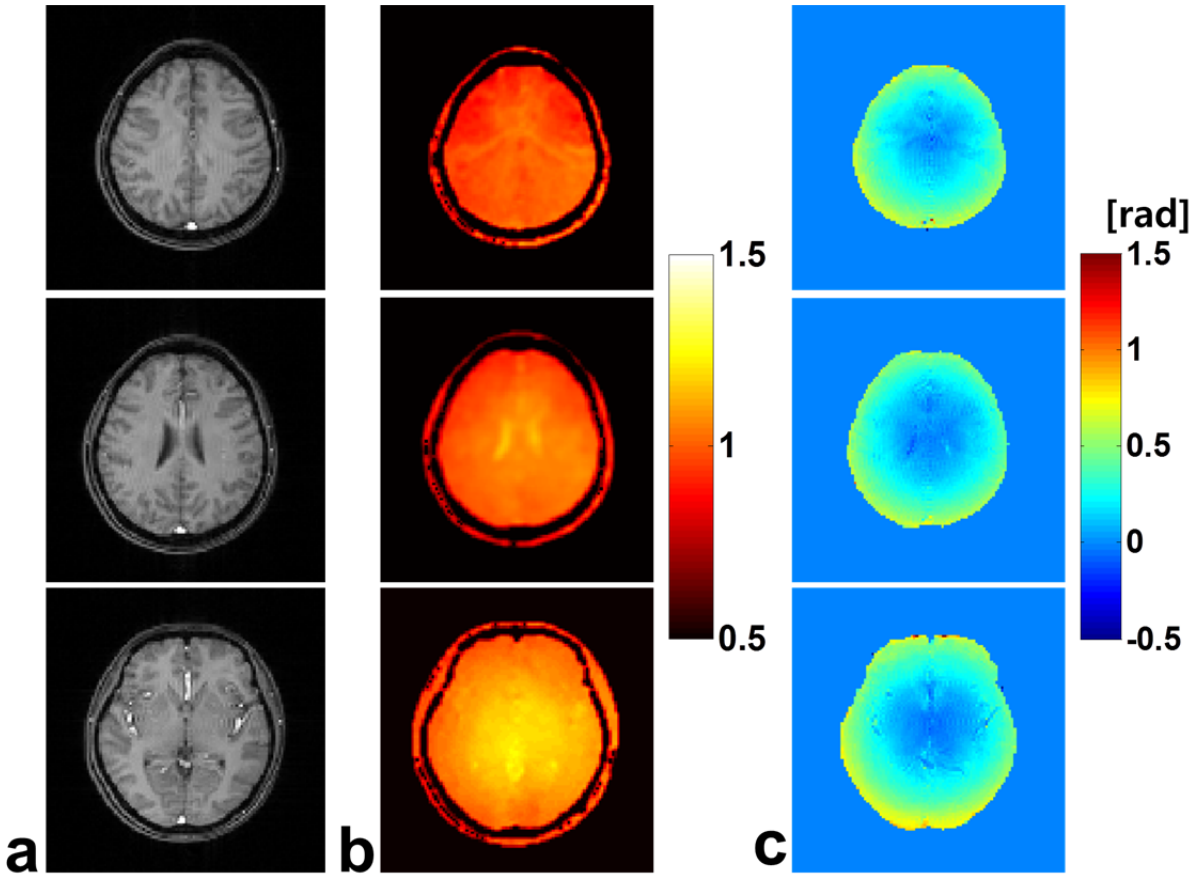

Figure 2. 6 *In vivo* human brain images obtained by the proposed DA-AFI method. **a:** Magnitude image of the DA-AFI, **b:** B_1^+ magnitude map, **c:** B_1^+ phase map.

2.4 Discussion and conclusion

Combining the multi-echo gradient echo sequence with the AFI method, a strategy to acquire 3D data has proposed and developed for measuring B_1^+ magnitude and B_1^+ phase map simultaneously with fast scan time. Furthermore, the flip angles were modified such that the second flip angle was twice the first flip angle to enhance the signal obtained from the second RF pulse. This technique estimates B_1^+ magnitude using the first gradient echoes acquired at both TRs (S_1, S_2). The B_1^+ phase map was obtained by linear fitting the multiple echoes acquired at the second TRs.

Fast scan time provides many advantages such as less movement of the imaging object and improvement of patient's convenience. Also, DA-AFI can image whole-body regardless of human body part. Therefore, this method can be used to a B_1 shimming preparation pulse or can visualize the RF field during the RF ablation [53]. This method can be applied to other clinical applications which need to estimate the RF field with fast scan time.

In this study, the intrinsic error of B_1^+ magnitude and phase mapping was calculated according to equations (2.10) and (2.12), respectively. The main assumption of the proposed method is that $TR_{1,2}$ are shorter than T_1 relaxation time for the first-order approximation. The region with short T_1 species will result in an overestimated B_1^+. The performance of B_1^+ mapping is also affected by various factors including T_1, ratio of TR_1 to TR_2 (*n* in equation 2.1), SNR, etc. The effect of these factors shows similar pattern in common AFI method. In DA-AFI, the dynamic range of signal ratio (S_2/S_1) was varying 0 to 2 with the change of flip angle. Signal ratio is sensitive to the variation of flip angles and this result in two times higher dynamic range than AFI method, for that reason DA-AFI provides a more accurate $\hat{B}_{1mag}$ map. In B_1^+ magnitude mapping, the increase of *n* causes the reduction of the intrinsic error of equation (2.1). Considering the scan time, the recommended *n* is in a range of 5-6.

For B_1^+ complex mapping, the flip angles are recommended to be 30°~50° for DA-AFI (n=5). The range of flip angles can be adjusted by the increase of n and r.

The AFI sequence is sensitive to unspoiled transverse magnetization. Therefore, a strong spoiling gradient is indispensable. For TR_2, the total spoiling gradient area was n times larger than that of TR_1. In this study, the multi-echo data was acquired only from TR_2 to guarantee sufficient spoiling time and spin relaxation. However, multi-echo data can be acquired at TR_1 if there exists enough time for a readout gradient. These additional multi-echo data could improve the accuracy of B_1^+ phase map. Using the multi-echo data, B_0 map estimation is possible without additional scan time.

The performance between common AFI and proposed DA-AFI was compared according to flip angle. DA-AFI was more robust to noise in estimating the B_1^+ complex map. In this study, DA-AFI had a higher SAR burden than conventional AFI. Although low flip angles less than 90 degrees were used for α and 2α, SAR was not a critical issue. Also, DA-AFI did not cause any SAR problems during the MR imaging. This enables analysis of mapping accuracy without being affected by SAR.

The proposed method was implemented based on a gradient echo sequence. Therefore an intrinsic limitation appears in regions of high B_0 inhomogeneity, such as air-tissue interfaces having severe signal loss. Although SNR of phase data can be improved using multiple echoes, this may not be beneficial since the effects of B_0 inhomogeneity increase along with TE. According to simulations, the optimal fitting echo was related to T_2* when a linear function are applied. The minimum noise standard deviation values was different at various T_2* species and were related to the SNR of multi-echo images. Also, the high-order B_0 inhomogeneity term cannot be removed even though application of the proposed linear algorithm [54]. To create a more accurate and robust B_1^+ phase map, additional complex and

time-consuming processes, such as high-order shimming, polynomial fitting, and filtering, are needed.

For B_1^+ phase mapping, blood flow causes a problem in estimating the initial phase. The phase of the flowing blood does not necessarily evolve linearly. Therefore, the linear fitting algorithm is not suitable to estimate the phase contribution of flowing blood. Future studies should address the flow effects in B_1^+ phase mapping.

A multi-echo sequence uses repeated readout gradients. Therefore, the phase of the image can be affected by eddy currents, which vary spatially. Presented data did not show effects of these components. Methods to remove gradient-induced eddy currents have been proposed [55, 56] and can be incorporated into proposed scheme. However, if the induced phase is a linear function of time, it can readily be resolved by the proposed method, which uses a linear fitting algorithm with equidistance echo intervals.

Chapter 3

Non-invasive *in vivo* Loss Tangent Imaging: Thermal sensitivity estimation at the Larmor frequency

3.1 Introduction

Hyper-thermic ablation is widely used therapeutic tool for treatment for cardiac arrhythmias and cancers of liver, lung, kidney, and bone [57-60]. Hyperthermia treatment uses thermal sensitivity difference between tumor and normal tissue. The thermal sensitivity is primarily determined by the dielectric properties such as electrical permittivity and conductivity. Relative permittivity denotes the ability to store electrical energy and conductivity including complex permittivity describes how well a material absorbs electromagnetic wave energy.

In the conversion of electromagnetic energy to thermal energy process, the dominant source of the heat is the electrical current density (J_c) due to the ohmic loss. The electrical conductivity of tissue, therefore, is used to estimate the quantity of the absorbed energy into the body such as calculate specific absorption rate. However, as the frequency of the electromagnetic wave becomes higher, displacement current (J_d) also influence the heating process due to a polarization. Therefore, permittivity should be considered in predicting temperature elevation. The effects of both conductivity and permittivity can be observed simultaneously using the dielectric loss tangent which is characteristic of materials.

The loss tangent ($\tan \delta$) is defined as the ratio of electric current density to displacement current density.

$$\tan\delta = \frac{J_c}{J_d} = \frac{\sigma}{\omega\varepsilon_0\varepsilon_r} = \frac{Power_{dissipated}}{Power_{stored}} \tag{3.1}$$

where σ is the conductivity, ω is the angular frequency, ε_0 is the dielectric constant in vacuum (ε_0= 8.854*10^{-12} F/m), and ε_r is the relative permittivity. It can be speculated that the loss tangent describes how efficiently electromagnetic wave energy is converted to thermal energy. Equation (3.1) can be rewritten using SAR.

$$\tan\delta = \frac{SAR \cdot mass}{Power_{stored}}, \quad where\ SAR = \frac{Power_{dissipated}}{mass} \tag{3.2}$$

From equation (3.2) it can be assumed that SAR has a positive correlation to the loss tangent. The SAR was used to predict the elevation of temperature while it considers only conductivity of tissues. Since loss tangent observes conductivity and permittivity, loss tangent can be a good complement to predict the temperature change. Predicting temperature elevation and measuring the quantity of energy transformation are advantageous in controlling hyper-thermic ablation. Still, monitoring and controlling the ablation volume are challenging and knowledge of the loss tangent can be beneficial in predicting the ablation volume. Exploring the effect of the loss tangent to the human tissue during these processes is valuable.

Recently, a novel non-invasive technique is introduced to estimate electrical properties named MREPT [3, 26, 39]. MREPT yields quantitative values for conductivity and permittivity determined at the MR Larmor Frequency. The conductivity and permittivity can be measured from RF field maps (generally termed B_1^+ map) using the Helmholtz equations. Therefore, loss tangent imaging can be performed using MREPT technique. Loss tangent imaging can also be used as a supplementary tool, since MRI used to guide treatments and surgeries in monitoring the temperature and visualizing tumors [61-65].

Most of the studies measured the *ex vivo* electrical properties or were performed on animals, because the measurement techniques are invasive. Previously, imaging the loss tangent property of biological tissue has been difficult, and non-invasive *in vivo* imaging of this property has yet to be performed.

In this study, a nondestructive loss tangent imaging method is proposed as an application of MREPT technique. The B_1^+ map which is necessary to measure the electrical properties was estimated using DA-AFI method. The loss tangent is visualized non-invasively using 3T MRI. The loss tangent could be considered that it reflects the conversion efficiency from electromagnetic wave energy to thermal energy. Temperature elevation could be predicted using loss tangent before the hyper-thermic process. To validate the potential of a loss tangent as a tool for thermal sensitivity mapping, numerical simulation was performed with various conditions. Especially, the effect of loss tangent in the process of hyperthermia which is performed at high frequency over the 900MHz was analyzed, since the temperature elevation was correlated with loss tangent at the high frequency while correlated with conductivity at the low frequency.

3.2 Methods

3.2.1 Simulations – Effect of loss tangent

The effect of loss tangent was observed using EM simulations to study the extent of the loss tangent as a monitoring parameter in the process of hyperthermia. Temperature variation, heat transformation, penetration depth were observed for a simple phantom model assuming hyperthermia. EM simulations were performed using the Bessel boundary matching (BBM) method [66] which can compute analytic solutions of electric and magnetic fields in a short

computation time. This method was implemented in Matlab. The boundary matching was performed in the Fourier domain. Built-in functions are used to calculate the Bessel coefficients. The Larmor frequency is set to 128 MHz as a frequency of 3T MRI. A single tissue phantom was designed with a circle shape with 10 cm in diameter (figure 3.1a). The phantom was considered to be a 2-dimensional cylinder model. An ablation antenna was assumed to be put into the center of the tissue. The magnitude of B_1^+ and E_z (z-component of the electric field calculated by BBM method) were estimated from simulations and SAR was calculated using E_z and dielectric property information ($SAR = \sigma E_z^2 / mass$).

Temperature elevation around the antenna was determined by measuring the peak value of local SAR. The temperature variation with respect to ablation frequency was observed by varying conductivity and permittivity at four different frequencies (Conductivity: 0.1~2.9 S/m, relative permittivity: 40~80, frequency: 460 kHz, 128 MHz, 915 MHz, 2.45 GHz).

In the second simulation, the efficiency of heat transformation was predicted by measuring the ratio of whole body SAR (sum of the SAR in the whole phantom) to the energy density in the dielectric medium ($\varepsilon E^2/2$). Also, the effective penetration depth was estimated by determining full width at half maximum (FWHM) of the local SAR around the antenna. Permittivity and frequency were varied with fixed conductivity (Conductivity: 0.7 S/m, relative permittivity: 32~80, frequency: 3 MHz~2.45 GHz) to observe how the permittivity affects the hyperthermia process.

3.2.2 Tissue loss tangent imaging – MREPT

MREPT yields quantitative values for conductivity and permittivity at the MR Larmor Frequency (128MHz at 3T MRI). The electric properties are estimated by analyzing complex B_1^+ map using the Helmholtz equations (3.3) and (3.4).

$$\sigma(x) \approx \mathrm{Re}\left(\frac{\nabla^2 B_1^+(x)}{j\omega\mu B_1^+(x)} \right) \tag{3.3}$$

$$\varepsilon_r(x) \approx \mathrm{Im}\left(\frac{\nabla^2 B_1^+(x)}{j\omega^2\mu\varepsilon_0 B_1^+(x)} \right) \tag{3.4}$$

where μ is permeability. In the above calculations, a smooth mollifier was applied. A kind of filter and the kernel size of filter can be adjusted with image SNR and geometry of phantom or tissues. In the phantom study, a Gaussian filter was used with kernel size of 3 and standard deviation of 1 to reduce the noise. A weighted second-order fitting algorithm was used for *ex vivo* data to reduce the boundary artifact around tissues. The tissue loss tangent image was determined from estimated conductivity and permittivity value maps (equation (3.1)). The electrical properties in each tissue were measured in the ROI (region of interest) which was selected a region of each tissue except boundary artifacts.

3.2.3 Sequence – Image acquisition

DA-AFI method was used to acquire the complex B_1^+ map, both magnitude and phase [67]. The details of this algorithm are introduced in chapter 2. The magnitude of B_1^+ is calculated using the equation (2.1). B_1^+ phase was estimated using a multi-echo acquired at TR_2 through linear least squares fitting. The approximation that the B_1^+ phase is half value of the transceive phase value was used [1, 26, 27].

3.2.4 Experiments

A phantom with different loss tangent values was built and used to demonstrate the performance of proposed method. Phantom was made as shown in figure 3.4a. Four regions were filled with varying concentrations of copper sulphate ($CuSO_4$) as a permittivity modifier and sodium chloride (NaCl) as a conductivity modifier to generate different permittivity and

conductivity. To prevent a water fluctuation inside the phantom, the aqueous solutions were solidified using agar powder. Axial images of the phantom were acquired on a 3.0T MRI scanner (Siemens Tim Trio) using a transmit-receive head coil. Applying DA-AFI, fourteen slices were obtained in 3D with resolution =2.0 × 2.0 × 4.0 mm^3, TR_1/TR_2= 20/100ms, first echo time = 3.55 ms, echo spacing = 3.55 ms, FA_1/FA_2 = 40/80°, FOV = 256 × 256 mm^2, number of echoes = 3, NEX = 3 leading to a total scan time of 10 minutes 45 seconds.

Ex vivo porcine shoulder imaging experiment was performed. The shoulder was soaked in water. DA-AFI pulse sequence was used to obtain complex B_1^+ map. Eighteen slices were obtained in 3D with resolution =2.0 × 2.0 × 4.0 mm^3, TR_1/TR_2= 30/150ms, first echo time = 3.55 ms, echo spacing = 3.55 ms, FA_1/FA_2 = 40/80°, FOV = 204 × 256 mm^2, number of echoes = 4, NEX = 3 leading to a total scan time of 16 minutes 33 seconds.

3.3 Results

3.3.1 Simulation

Simulation results are shown in figure 3.1. Since the ablation antenna located the center of the tissue, RF propagates from center to boundary region. The pattern of wave propagation was estimated to be dependent on the conductivity and permittivity. In the dielectric medium, the ablation frequency becomes higher with increasing permittivity and lower with increasing conductivity (figure 3.1d).

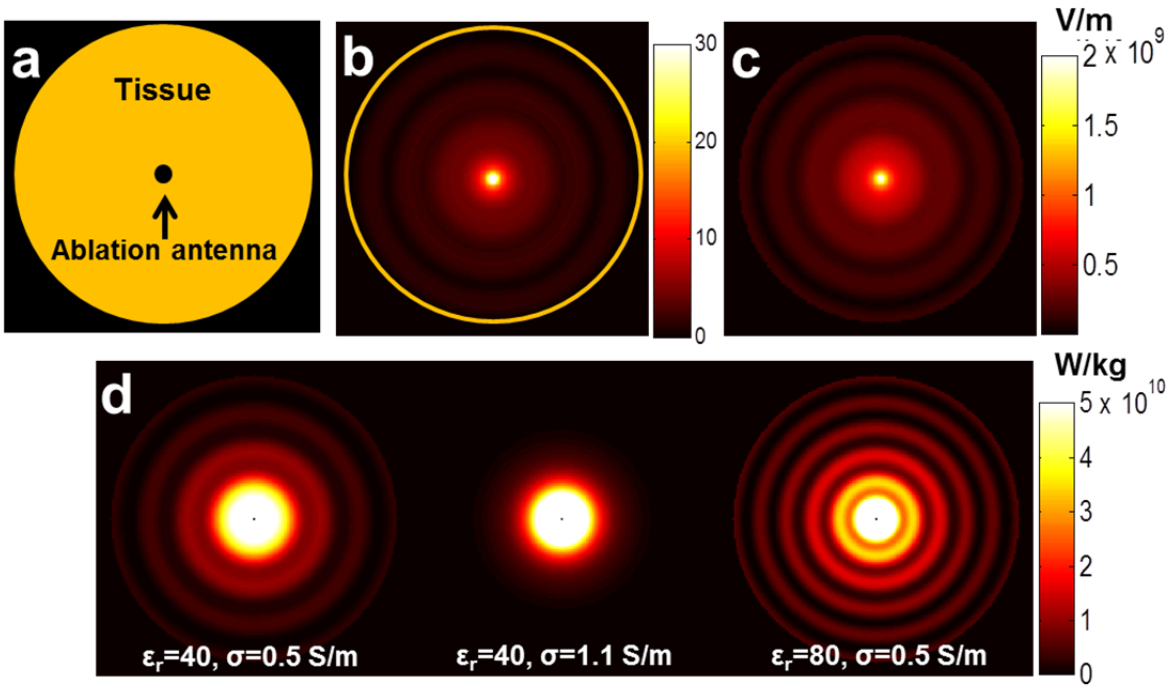

Figure 3. 1 Simulation results performed at 915MHz. **a:** Phantom design, **b:** B_1^+ magnitude, yellow ring denotes the tissue boundary and the ablation antenna is put into the center of the tissue, **c:** E_z (ε_r=40, σ=0.5 S/m), **d:** SAR (Electrical properties are noted on each figure.). Z-axis is represented by the through-plane direction.

Figure 3.2 displays the peak local SAR with respect to conductivity and permittivity. The four figures show the tendency of temperature variation with respect to ablation frequencies. Figure 3.2a and 3.2b show that the peak local SAR values are directly proportional to the conductivity. The peak local SAR values, however, are more proportional to the loss tangent in figure 3.2c and 3.2d. From this, the conductivity can be used to predict temperature variation at low frequency ranges used in RF ablation (<~300MHz) while the loss tangent can be the dominant parameter in predicting temperature elevation at high frequency ranges used in the microwave ablation (>~1GHz).

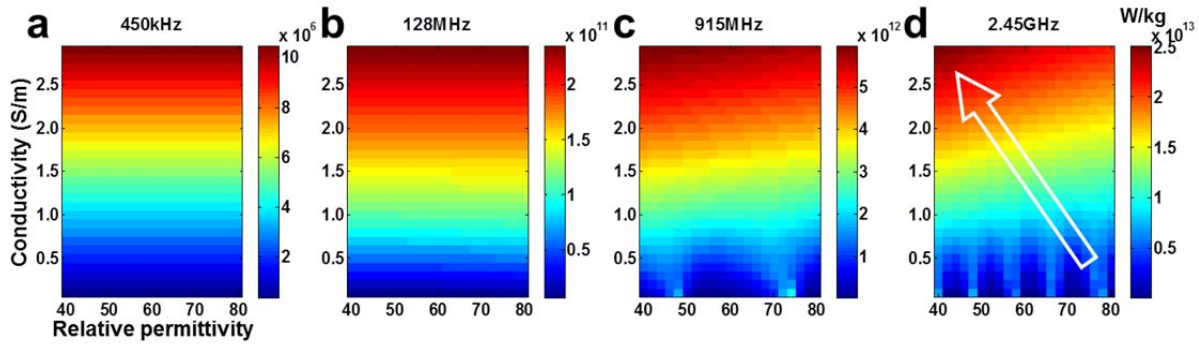

Figure 3. 2 Simulation results showing peak local SAR. To observe a dominant factor to elevate temperature, simulation was performed with four different ablation frequencies. At low frequency ranges used in RF ablation, the temperature is directly proportional to the conductivity (a, b). However, in high frequency ranges used in the microwave ablation, temperature elevation is proportional to the loss tangent (c, d). The loss tangent increases through the direction of the white arrow.

The results of second simulation are shown in figure 3.3. The line plot, figure 3.3a, shows that the efficiency of heat transform is increased with the loss tangent increment. In figure 3.3b, the FWHM of the local SAR is decreased with increasing ablation frequency and relative permittivity. It can be concluded that the energy efficiency and the effective penetration depth have positive correlation with the loss tangent values.

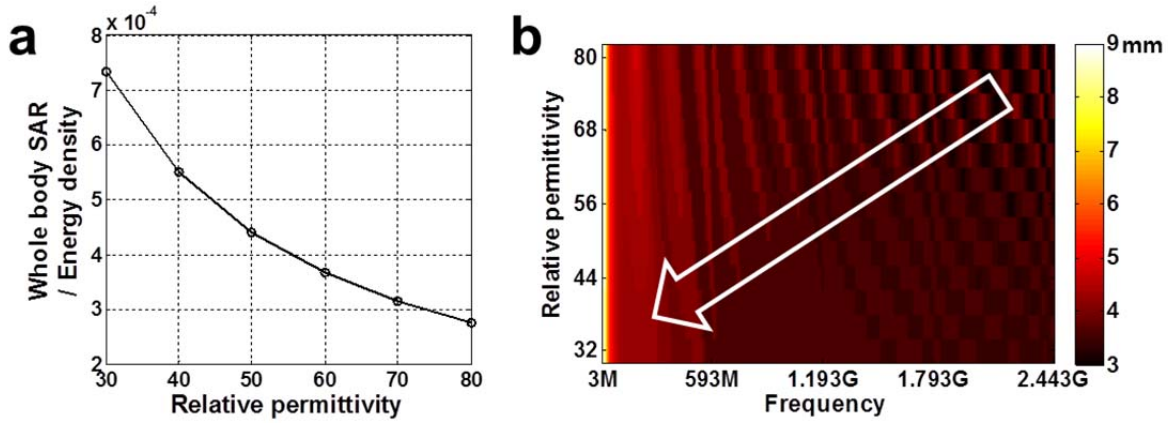

Figure 3. 3 a: Line plot of the heat transform efficiency. The heat transform efficiency (ratio of whole body SAR over energy density) is decreased with increasing relative permittivity (decreasing loss tangent). **b:** Full width at half maximum of the local SAR. FWHM of the local SAR is decreased with increasing ablation frequency and relative permittivity (Conductivity: 0.7 S/m). Therefore, the penetration depth is proportional to the loss tangent. The loss tangent increases through the direction of the white arrow.

3.3.2 Phantom study

Figure 3.4 shows phantom imaging results. As expected, the conductivity and permittivity images (figure 3.4b-c) have strong correlations with the ion concentrations. However, differences between $CuSO_4$ and NaCl concentrations are not clearly shown in figure 3.4b-c. The loss tangent image represents distinct contrast to each specific region. Table 3.1 represents the estimated electrical properties of the phantom. The literature values of conductivity and permittivity with respect to each concentration of NaCl and $CuSO_4$ aqueous are shown in Table 3.2 [68-71]. Quantitative electrical property values match well with concentrations of NaCl and $CuSO_4$. The decrease in ε and the increase in σ with respect to the NaCl and $CuSO_4$ concentrations were observed. The loss tangent value is also calculated using equation (3.1).

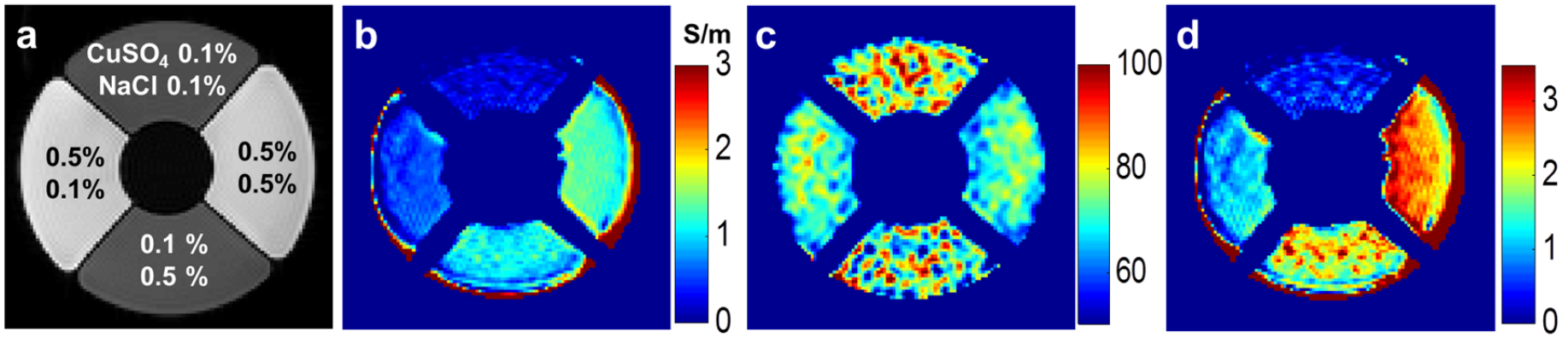

Figure 3. 4 Results of the phantom study. **a:** MR image and the concentrations of $CuSO_4$ and NaCl are noted at each chamber, **b:** Conductivity image, **c:** Relative permittivity image, **d:** Loss tangent image. The loss tangent image represents distinct contrast to each specific region. Since, the permittivity processing is more sensitive to the noise, the estimated permittivity map has larger standard deviation than the conductivity map.

Table 3.1. Estimated electrical properties

($CuSO_4$, NaCl)(%)	**σ (S/m)**	**ε_r**	**tan δ**
(0.1, 0.1)	0.26±0.13	78.56±10.31	0.48±0.24
(0.5, 0.5)	1.33±0.07	70.65±5.15	2.61±0.36
(0.1, 0.5)	1.11±0.14	74.42±11.68	1.93±0.49
(0.5, 0.1)	0.53±0.10	71.73±5.37	1.14±0.26

Table 3.2. Literature values (25°)

Concentration (%)		**σ (S/m)**	**ε_r**
$CuSO_4$	0.1	0.06	78.19
	0.5	0.29	77.68
NaCl	0.1	0.16	78.75
	0.5	0.82	77.75

3.3.2 *Ex vivo* biological tissue imaging experiments

Figure 3.5 shows results of the *ex vivo* study. The images were masked to remove a disturbance from uncertain tissues. Conductivity and permittivity of the fat show low intensity compared to red meat. Loss tangent image, however, shows different contrast. The fat and red meat have similar loss tangent values. The estimated values are represented in Table 3.3. These results show that not only conductivity but also permittivity should be considered to monitor the temperature change at high frequency.

Many artifacts (yellow arrow) appeared due to the complex structure of the tissues. Also, inhomogeneous tissue composition is not suitable for MREPT process since MREPT assumed the tissues are homogeneous. The insufficient SNR and insufficient number of voxels to estimate dielectric properties are sources of artifacts occurred at the boundary of fat. The right arrow indicates artifacts may come from the regional sources. B_1^+ map would be hampered due to the B_0 inhomogeneity since this region is adjacent to the end of the coil.

Table 3.3. Estimated electrical properties

Tissue type	**σ (S/m)**	**ε_r**	**tan δ**
Fat	0.30±0.16	39.56±11.60	1.16±0.95
Red meat	0.63±0.13	75.80±10.10	1.20±0.40

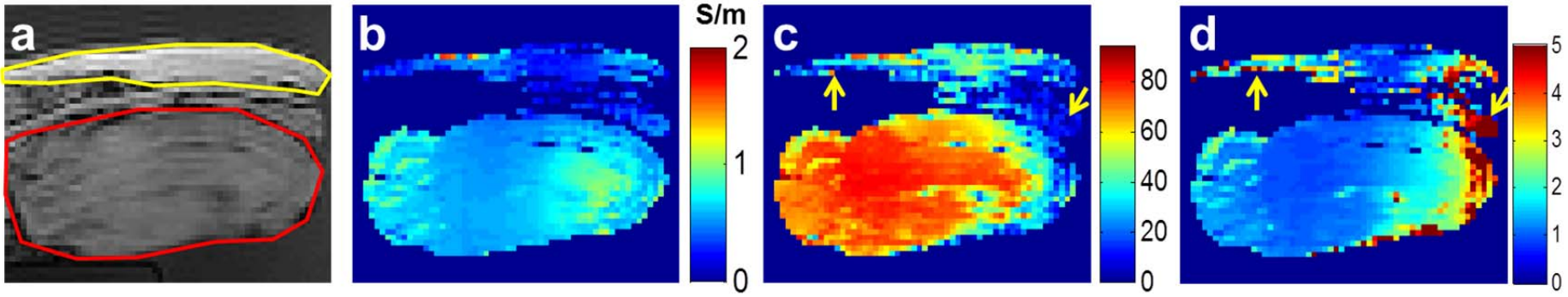

Figure 3. 5 *Ex vivo* experiment results (shoulder of a pig). **a:** MR image. Fat is delineated with a yellow line and red meat is delineated with red line. **b:** Conductivity image, **c:** Relative permittivity image, **d:** Loss tangent image. Conductivity and permittivity of the fat (σ: 0.30±0.16 S/m, ε_r: 39.56±11.60) show low intensity compared to red meat (σ: 0.63±0.13 S/m, ε_r: 75.80±10.10). Loss tangent image, however, shows different contrast (red meat: 1.20±0.40, fat: 1.16±0.95). The fat and red meat have similar loss tangent values. Artifacts (yellow arrow) appeared due to the complex structure of the tissues, inhomogeneous tissue composition, insufficient SNR, and insufficient number of voxels to estimate dielectric properties.

3.4 Discussion and conclusion

In this study, the potential of loss tangent imaging was proposed to be a tool for predicting the RF wave propagation in the context of hyperthermia. The loss tangent image represents the interaction between the human tissue and the electromagnetic fields. The advantage of loss tangent imaging is in providing a new contrast mechanism which reflects the thermal sensitivity of human tissues. Non-invasive loss tangent was measured from the complex B_1^+ map using MREPT algorithm. The loss tangent image was successfully reconstructed in the phantom study.

The effect of the loss tangent was investigated with simulations. The relation between loss tangent and thermal sensitivity were observed. Especially, in high frequency ranges as those used in the microwave ablation, loss tangent becomes a major predicting factor in determining thermal sensitivity. Relationships with the heat transform efficiency and effective penetration depth were also investigated, which are important factors in the control of the ablation volume. It may be a usable marker for thermotherapy applications.

In the simulation results of Fig. 3.2-3, a pulsatile pattern was revealed which is due to resonance. The resonance occurs when the oscillation frequency matches the natural vibration frequency of the material. At these resonance frequencies which are at half the wavelength, the material absorbs more energy than at other frequencies. The wavelength becomes shorter with the increase of RF frequency and permittivity of material. Therefore, the pattern becomes denser according to the increase of ablation frequency and tissue permittivity.

Dielectric properties of the tissues have frequency dependence. Typically, permittivity is continuously decreased and conductivity is increased with frequency for soft tissues [31, 65]. Most of the electromagnetic dosimetry study measured a spectrum in the broad frequency range, from several Hz to GHz. However, the proposed method measured loss tangent at only

the Larmor frequency because MRI was used to imaging loss tangent. This shortage can be overcome to use multiple Cole-Cole expression [72] which is used to interpolate the spectrum of loss tangent [73].

In actual hyperthermia, the electrical properties of the background tissue also affect RF heating [74]. The electrical conductivity of each tissue determines the current pathway and current density. In this study, a simulation phantom was designed that composed one homogeneous tissue for clarity and simplicity to observe the effect of the loss tangent. Additional simulation should be performed in many situations for determining the ablation efficiency and the temperature elevation.

MREPT process is sensitive to noise due to the Laplace operator. Recently, various post processing methods such as weighted polynomial fitting, median fitting, and bilateral filter have been developed to obtain accurate electrical property maps [3, 75]. Smoothing filter such as Gaussian filter is the most frequently used technique to reduce noise from acquired data. Weighted polynomial fitting method can improve the quality of the electrical property maps and significantly reduce the boundary artifact occurring at boundary of different tissues. Conventionally, a smooth filter is applied to reduce the noise to the homogeneous region while a fitting algorithm was used to *ex vivo* or *in vivo* experiment due to the complex geometry. The electrical property estimation of the biological tissue is a challenging work. SNR is a one of limitation factor when applying this technique to biological tissues. Further improvements of MREPT technique are needed.

Chapter 4

Flow effect removal and phase correction within the flow component for conductivity estimation

4.1 Introduction

Imaging the electric property of tissues can potentially provide new contrast for the diagnosis of various diseases [29, 36, 76]. In this thesis, the electrical properties were measured using complex B_1^+ map. In particular, to calculate the electrical conductivity, accurate measurements of the B_1^+ phase are needed. The phase information of the B_1^+ is frequently distorted due to the flow components which include capillary, vessel, and even cerebrospinal fluid (CSF) flow.

Electrical conductivity of the blood is interested to monitor the hemodynamic [32, 77-79]. The conductivity of blood is measured using impedance meter and blood suspension are modeled by the Maxwell-Fricke equation [80]. Many studies find that the conductivity of flowing blood is changed due to flow [32, 41, 81]. In MRI, the phase distortion due to flow propagates and significantly degrades the conductivity estimation. Therefore, a preconditioning is needed to limit the phase perturbation from flow in order to get a conductivity map without flow effects.

For static tissues, zeroth-order moment accumulates when encoding gradients are applied and this moment is compensated by refocusing gradients. However, for moving spins such as laminar flow, uncompensated first-order moments of encoding gradient remain and cause unwanted image artifacts. Imaging sequence can be modified with the use of additional

gradient to compensate the phase distortion from the moving spins [82]. These flow compensation techniques such as gradient moment nulling [83, 84] can be used to remove the undesired phase accumulation coming from flow.

Simple technique to remove flow effect is an application of double spin echo [85]. Phase cancellation occurs at every even echo due to spin rephasing since the movement of laminar flow is coherent. Hence, reduction of ghosting is observed at even echo images of the double spin echo sequence.

After removal of undesired effects, the flow signal contains information regarding the source of dynamic components information such as blood flow and cardiovascular function [86]. Quantitative flow measurement can be achieved by phase-contrast (PC) MR imaging. In phase-contrast methods, moving spins are imaged by applying flow encoding gradient [87, 88]. For moving spins, a phase shift is generated along the flow encoding gradient. This phase shift is proportional to the velocity of the moving spins. Therefore, after elimination of the phase shift generated by other sources, the velocity of motion can be calculated using the measured phase shift.

This study focuses on the reconstruction of *in vivo* conductivity map using flow compensated double spin echo signals and analyzes flow induced effects in B_1^+ phase to improve the estimation of electrical conductivity. This approach is studied with phantom and *in vivo* experiments.

4.2 Methods

4.2.1 B_1^+ mapping using double spin echo

Gradient moment nulling removes the ghosting artifacts in the magnitude image effectively. However, phase within the flow still has additional flow induced phase component [89]. A double spin echo sequence is used to remove the phase perturbation. The double spin echo sequence is described in figure 4.1. The first-order moment is $-\gamma G_x \Delta t^2$ at the first echo and zero at the second echo. Here, the G_x is the magnitude of the readout gradient.

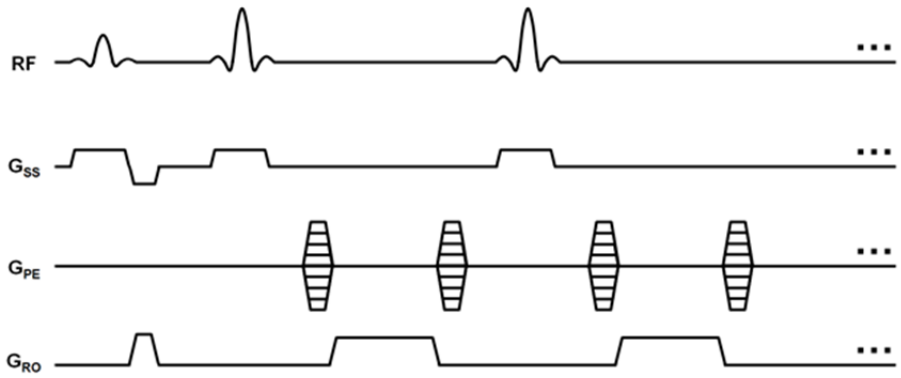

Figure 4. 1 Sequence diagram of a double spin echo sequence. The second echo provides nulled first-order moment. The first echo is same as a normal spin echo image.

The standard B_1^+ mapping method can be used in the case of double echoes. In this work, the magnitude of the B_1^+ is determined by DAM which uses the signal ratios of images acquired using two different flip angles (α and 2α).

$$\alpha_{DAM} = \cos^{-1}\frac{S_2}{2S_1} \tag{1.5}$$

where S_1 and S_2 are signal intensity with different flip angle α and 2α, respectively. The phase of the B_1^+ is determined from phase information of a spin echo image.

4.2.2 Flow imaging

Flow causes phase difference and it linearly accumulates with respect to velocity of the flow, therefore velocity map can be calculated using 2D PC acquisition. Two sets of image were acquired using bSSFP sequence with and without flow and then phase difference was calculated between the two images. To remove phase perturbation inside the flow component, a spatial polynomial fitting is performed on the phase difference image. Using the fitted coefficients and velocity map which were acquired using 2D PC technique, the B_1^+ phase with flow component can be corrected within the ROI region. The phase of the B_1^+ is determined from phase information of a bSSFP image.

4.2.3 Conductivity imaging

The conductivity (σ) is measured from B_1^+ phase map using the Helmholtz equation

$$\sigma(r) = real\left(\frac{\nabla^2 B_1^+(r)}{i\omega\mu B_1^+(r)}\right) \tag{3.3}$$

where μ is permeability, and ω is the angular frequency.

Double spine echo experiment

In the MREPT process, a Gaussian filter with kernel size 5 and standard deviation 1 was used to reduce the noise. The kernel size was determined with SNR of the image to get a homogeneous conductivity map. Both B_1^+ magnitude and phase were used to calculate the conductivity.

Flow imaging experiment

A half of the bSSFP phase was used calculate to the B_1^+ phase and resulting B_1^+ phase was used to estimate the conductivity mapping. In this experiment, a straw is put into the phantom to mimic a vessel structure. A number of voxel inside the straw is smaller than other tissues,

fitting algorithm was used to estimate the electrical conductivity. A weighted second-order fitting algorithm was applied experimental data to reduce the boundary artifact among tissues. Median filter with kernel size 3 was used to reduce impulse noise before conductivity estimation.

4.2.4 Imaging experiments

A vessel mimicked phantom was made as shown in figure 4.2. Background region except inside the straw was filled with NaCl aqueous solution having conductivity value of 1.9 S/m. The diameter of straw was 11 mm. Through the straw, NaCl solution was pumped into the pipe by a motor pump with a certain velocity (50 m/s). A bottle of the NaCl aqueous solution which was pumped into the straw was also imaged as a reference.

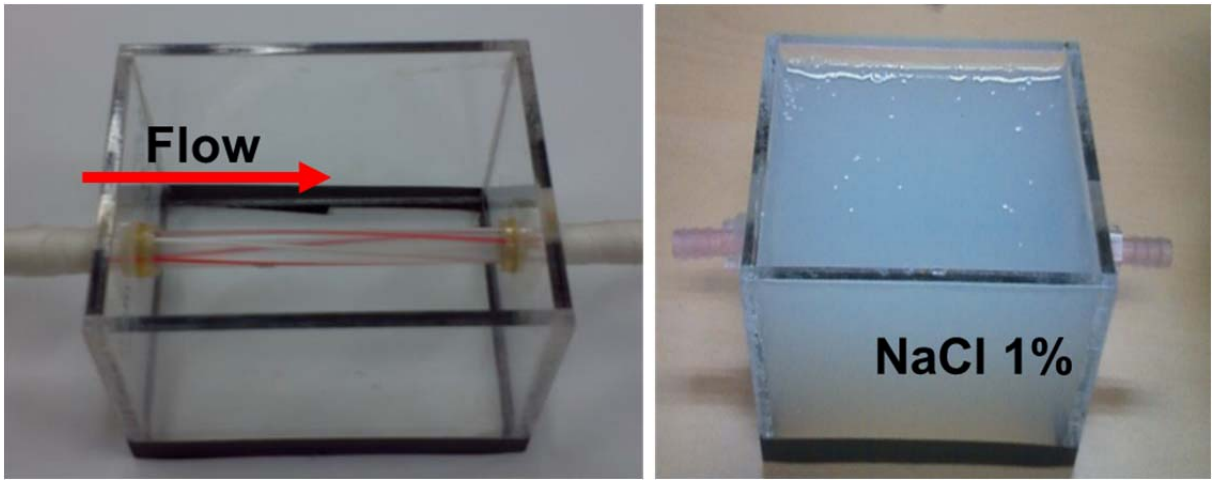

Figure 4. 2 A vessel mimicked phantom. Background region has 1.9 S/m conductivity value. The diameter of straw was 11 mm. NaCl aqueous solution was pumped into the straw.

Double spin echo experiment

Phantom and *in vivo* experiments were performed using the double spin echo sequence.

In the phantom experiments, the flowing solution had 4.9 S/m conductivity value. Axial images of the phantom were acquired on a 3.0T Siemens Tim Trio MRI scanner using a transmit-receive head coil. For B_1^+ magnitude mapping, two consecutive scans are performed with $\alpha_1 = 60°$, $\alpha_2 = 120°$ and 180° for all of the refocusing pulses. Six slices were obtained in 2D acquisition mode with resolution 1.5 × 1.5 × 4.0 mm^3. Although large voxel size is preferred to achieve high SNR, 1.5 mm was chosen in order to guarantee sufficient number of voxels inside the straw. The double spin echo sequence with TR = 5000 ms, TE_1 = 12 ms, TE_2 = 24 ms (twice of TE_1), and FOV = 96 × 196 mm^2 was used, leading to a total scan time of 32 min at each scan.

In vivo experiment was performed with a healthy normal volunteer. Sagittal images were acquired using a transmit-receive head coil. Four slices were obtained in 2D acquisition mode with resolution 2.0 × 2.0 × 5.0 mm^3. The double spin echo sequence with TR = 2000 ms, TE_1 = 8.8 ms, TE_2 = 17.6 ms (twice of TE_1), FOV = 256 × 256 mm^2, NEX = 4 was used, leading to a total scan time of 17 min at each scan.

Flow imaging experiment

Phantom experiment was performed. The flowing solution conductivity was 1.9 S/m (same as a conductivity of background region). Axial images of the phantom were acquired using a transmit-receive head coil. Two sets of image were acquired with and without flow. The parameters of the bSSFP sequence were resolution = 1.0 × 1.0 mm^2, slice thickness = 5 mm, TR/TE = 4.10/2.05 ms, FA = 70°, FOV = 128 × 128 mm^2, NEX = 8 leading to a scan time of 5.8 seconds. The 2D-PC image was scanned with same parameters except for the TR/TE = 15.80/4.37 ms, FA = 15°, VENC = 90 cm/s. The scan time was 3.5 seconds.

4.3 Results

4.3.1 Phantom study of double spin echo experiment

The magnitude and phase images are shown in figure 4.3 a-b, respectively. The left column represents the first echo images and the right column shows the second echo images. The ghosting artifact along the phase encoding direction is shown in first echo. The B_1^+ map and reconstructed conductivity map (figure 4.3 c-d, first column) is hampered by the ghosting artifact. For the second echo images, the ghosting artifact is significantly reduced and the conductivity map is reconstructed successfully at the homogenous region while the estimated conductivity of flowing signal is different from the reference solution. Since the flow signal is nulled at the second echo, the phase signal inside the straw has low SNR. Therefore, the reconstructed conductivity value inside the straw is regarded as noise. Source of the overestimated conductivity value near the wall of the straw is not only a flow signal but also a boundary artifact.

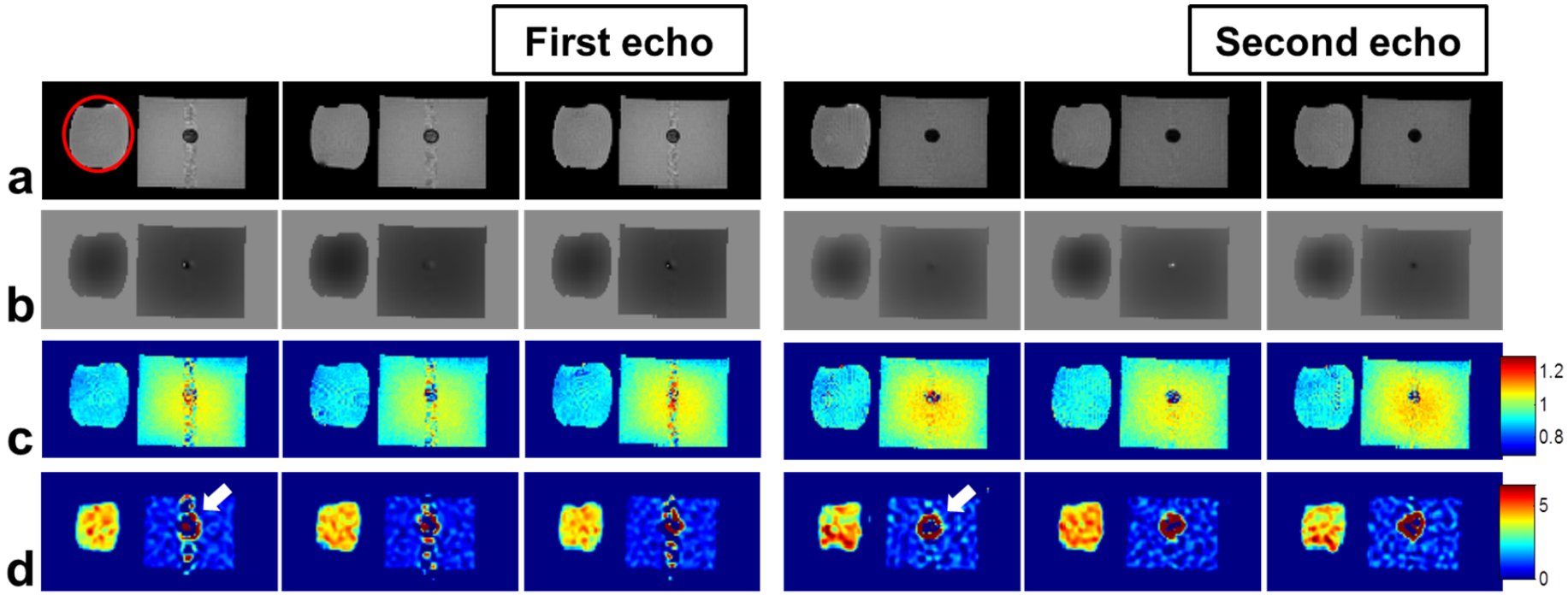

Figure 4. 3 Results of the phantom experiments. **a.** Acquired images using double spin echo sequence. Ghosting artifact is shown at the first echo images along the phase encoding direction while the flow effect is almost removed at the second echoes. The red circled signal is a reference of the flowing solution. **b.** Phase image of a double spin echo. The phase is also used as a B_1^+ phase. **c.** B_1^+ magnitude map measured by DAM method. **d.** Reconstructed conductivity map using MREPT technique.

4.3.2 *In vivo* study of double spin echo experiment

The results of *in vivo* study are shown at figure 4.4. Signal intensity becomes restored between the cerebrum and the cerebellum at the second echoes (red circled region). The increased intensity of the second echo's magnitude image compared to the first echo image is caused by the addition of stimulated echoes. This induces higher SNR without distortion of the phase information, which is an added benefit of using double spin echo. The pattern of B_1^+ magnitude shows that using the second echo is better in estimating the B_1^+ magnitude even though a relatively short TR was used. White arrows show distorted and restored regions by the signal attenuation caused by flow.

The B_1^+ magnitude signal varied depending on the brain geometry while normal B_1^+ magnitude smoothly varies. Conventionally, DAM method recommends long TR ($TR \geq 5 \times T_1$) to ignore the T_1 relaxation term. However, short TR (2000 ms) was used in this study due to a limitation of the scan time. Therefore, the T_1 contrast was remained at the ratio of images (S_2/S_1) and it causes B_1^+ magnitude mapping error.

The reconstructed conductivity is shown in figure. 4.4d. Using the phase of second echo to estimate conductivity shows better geometry of brain especially near the CSF than using the phase of first echo. Since brain has a complicated geometry and consisted of numerous tissues, the processing of MREPT is difficult. Although some boundary artifacts are smoothened by the Gausian filter, many artifacts remain in the conductivity map.

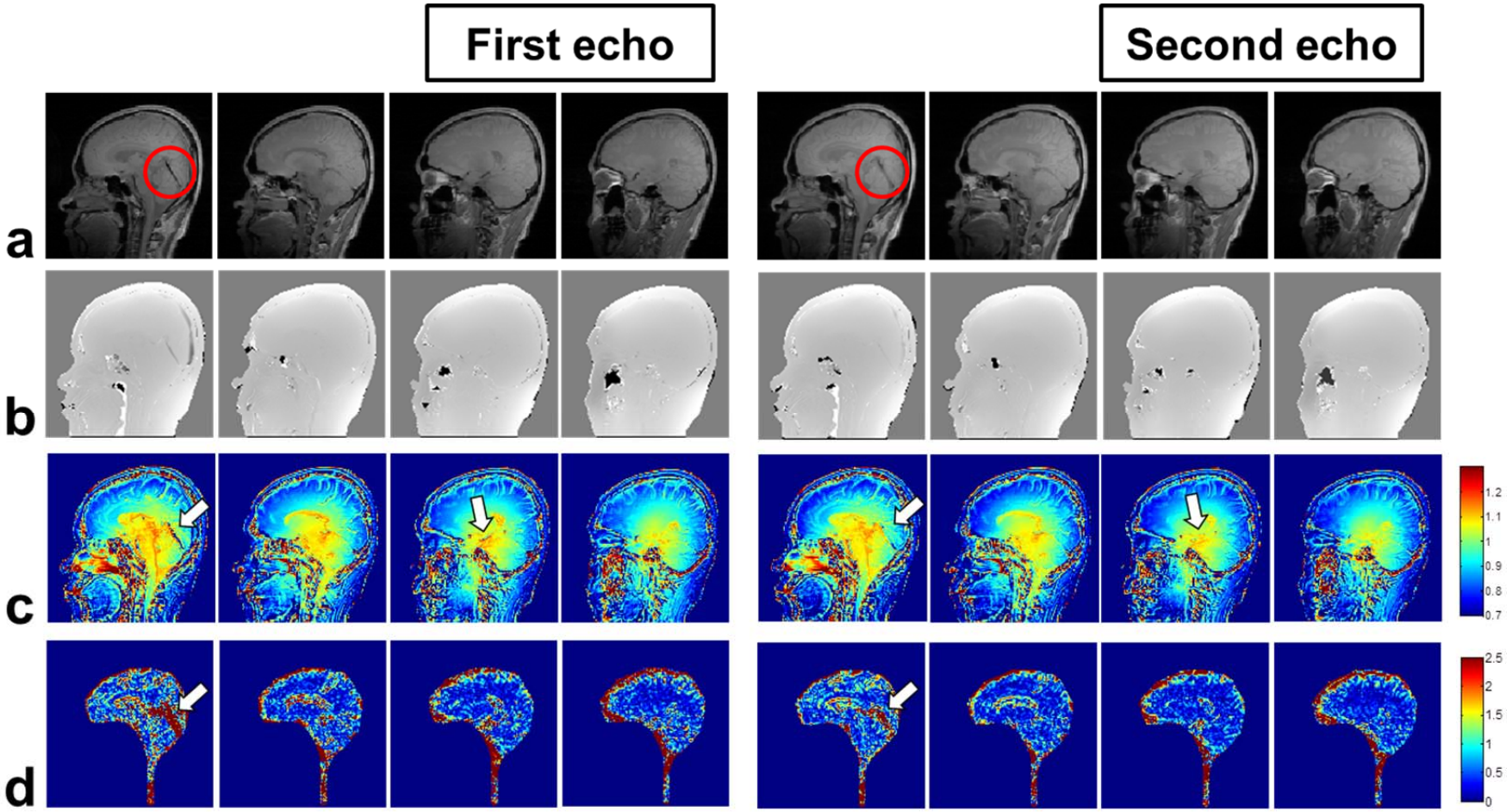

Figure 4. 4 Results of the *in vivo* experiments. **a.** Acquired images using double spin echo sequence. Signal intensity become restoration between the cerebrum and the cerebellum (red circled region). **b.** Phase image of a double spin echo. **c.** B_1^+ magnitude map measured by DAM method (Scale: [0.7, 1.3]). **d.** Reconstructed conductivity map using MREPT technique (Scale: [0, 2.5] S/m). White arrows show distorted and restored regions by the signal attenuation caused by flow.

4.3.3 Flow imaging experiment

Figure 4.5 shows the magnitude, phase and estimated conductivity images. Flow induced phase can be estimated to compare the two sets of data (with and without flow data). Additional phase was accumulated when the aqueous solution flows through; therefore the electrical conductivity was highly overestimated at the flowing region (w/o flow: 1.60 ± 0.05 S/m, with flow: 8.86 ± 0.46 S/m), while same conductivity values were estimated at both background regions (w/o flow: 1.59 ± 0.03 S/m, with flow: 1.55 ± 0.10 S/m). The scale was adjusted to express the overestimated conductivity. The measured conductivity was entirely underestimated compare to true conductivity. Lack of the B_1^+ magnitude can cause underestimation of the conductivity.

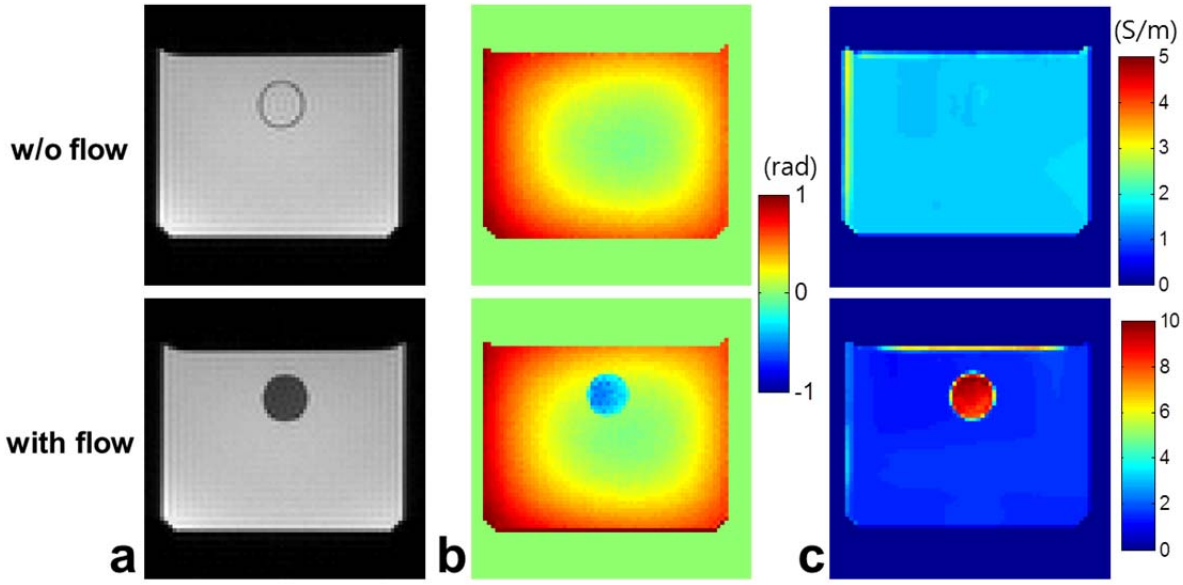

Figure 4. 5 Results of the phantom experiment. **a.** Acquired images with and without flow using bSSFP sequence. **b.** Half of the phase of the bSSFP image. This phase is used as the B_1^+ phase. Additional phase accumulation is observed in the flow image. **c.** Estimated conductivity maps. The electrical conductivity was highly overestimated at the flowing region, while same conductivity values were estimated at both background regions.

Since the phase difference (phase with flow – phase w/o flow) and velocity encoded map shows similar pattern (figure 4.6 a-b), the phase difference was fitted linearly by the velocity map which is acquired with 2D-PC acquisition. The measured average velocity was 60 m/s inside the straw. The flow induced phase was notably reduced after phase correction (figure 4.6 c) and the reconstructed conductivity value is close to real value (figure 4.6 d). The estimated conductivity inside the straw was 2.44 ± 0.01 S/m and background conductivity was 1.53 ± 0.02 S/m. At the boundary of straw, uncorrected phase was shown. Also, due to the low SNR of the velocity map, noise was significantly increased inside the straw. These factors cause estimation error of conductivity.

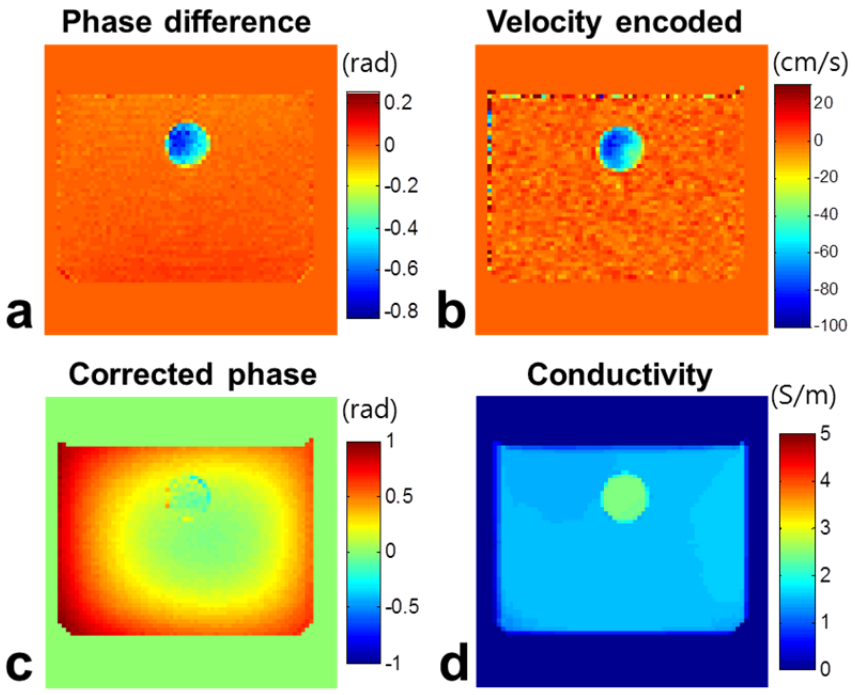

Figure 4. 6 Results of the phase correction. **a.** Phase difference map (phase with flow – phase w/o flow). **b.** Velocity encoded map which is acquired with 2D-PC acquisition. **c.** Corrected phase map. **d.** Conductivity map estimated using the corrected phase.

4.4 Discussion and conclusion

This study tried to estimate the conductivity of flow and proposed a double spin echo sequence to remove effects of flow from the conductivity. The double spin echo method removes the flow perturbation effectively from the whole image. The accuracy of estimated conductivity map is improved near the flow, since the ghosting artifacts are significantly reduced from the images and B_1^+ map.

Estimation of conductivity is inaccurate at the flow component due to additional flow induced phase. Balanced SSFP-based EPT approaches should take note of this factor in the presence of flow. I tried to remove the additional phase using spatial polynomial fitting. Since strong correlation between the phase difference of with and without flow signal and velocity encoded phase was observed, the velocity encoded phase which is acquired from a separate acquisition was used to the spatial polynomial fitting. This two-step process can correct for the flow related additional phase.

Flow induced phase follows a quadratic profile. The phase induced by conductivity is also expressed as a quadratic function, therefore, separation of the flow induced phase from the B_1^+ phase is impracticable using only a spatial polynomial fitting. The fitted coefficient would be correlated with echo time, local field variation and other extra terms. More dedicated approaches such as interleaving the flow encoding and non-flow encoding can provide a more robust method for phase correction.

Blood can be described as a suspension of ellipsoidal particles such as red blood cells in an electrolytic solution. The electrical conductivity of blood depends on the hematocrit (the volume fraction of red blood cells) and the conductivity of plasma which depends on the temperature, ionic content, and so on [41, 78]. Also, conductivity of blood contains information related to the velocity of the blood. The electrical conductivity of flowing blood was observed that the conductivity was increased in comparison to the conductivity of

stagnant blood [32, 81]. However, the electrical conductivity is not linearly proportional to the velocity of blood [90].

Many smoothing filter is used to reduce the noise, since MREPT process is sensitive to noise and the variation of tissues. However, the smoothing filter causes a partial volume effect at the boundary of tissues. To avoid partial volume effect, sufficient number of voxel in each homogeneous region should be guaranteed. Because most regions of existing flow such as blood vessel are small and narrow, the conductivity measurement of flow is difficult. In many cases, the conductivity values of flow are hampered by boundary artifact. In this study, therefore image acquired with higher resolution than other MREPT approaches.

Flow is assumed laminar flow which travels smoothly and undergoes regular paths. However, in the straw, flow perturbation exists at the entrance of the straw, the exit of the straw, and near the wall of straw. These could be eliminated using higher-order moment compensation with encoding gradients. Currently, higher-order moment remains at the B_1^+ phase, causing estimation error of conductivity.

The signal intensity was reduced when the spin is flowing or moving at both double spin echo and bSSFP data. Since SNR is an important factor to obtain accurate conductivity map, there are some limitations to estimate the conductivity of flow. Future studies could focus on moving spins even though the signal of static spins is damaged.

Chapter 5
Future directions

5.1 Complex B_1^+ mapping

5.1.1 B_0 inhomogeneity

Although the proposed method successfully measured the B_1^+ map, a fundamental limitation appears in the regions of severe signal loss due to high B_0 inhomogeneity since the approach was implemented based on a gradient echo sequence. Although optimal parameters were used, the accuracy of measured phase is insufficient to estimate the electrical properties. In terms of sequence development, the TE and ΔTE can be minimized to reduce the B_0 effect or the combination of flip angles can be changed to acquire higher SNR signal at the TR_2. However, the limitation of the gradient sequence still remains.

A z-shimming technique effectively recovers signal loss due to the macroscopic field inhomogeneity [91]. This technique reduces the phase dispersions induced by field inhomogeneity to adopt additional compensation gradients in the through-plane direction. Z-shimming technique is conventionally used to improve the performance of T_2* mapping which uses multi-echo gradient echo data. The z-shimming technique can be applied to the proposed method since DA-AFI also uses the multi-echo gradient echo data.

5.1.2 Linear fitting algorithm

A linear fitting algorithm was used to estimate B_1^+ phase. This algorithm reconstructed the initial phase successfully at the static tissues. However, the phase accumulates does not always have linear dependency with TE. For example, linear fitting algorithm is not suitable for estimation the phase contribution of flowing blood since the phase of the moving spins does not necessarily evolve linearly. Also, the phase induced by eddy current should be considered due to the repeated readout gradients. Schemes which compensate the high-order terms could be combined to the proposed sequence or technique [55, 56, 85, 92].

5.2 Loss tangent imaging

5.2.1 Spectrum of the loss tangent

The possibility of loss tangent imaging is proposed to be a tool for predicting the RF wave propagation in the context of hyperthermia. The motivation to perform loss tangent imaging is in providing a new contrast mechanism which reflects the thermal sensitivity of human tissues. The proposed loss tangent image represents the interaction between the human tissue and the electromagnetic fields at the Larmor frequency. Dielectric properties of the tissues have frequency dependence. Most of the electromagnetic dosimetry study measured a spectrum in the broad frequency range, from several Hz to GHz. However, the proposed method measured loss tangent at only the Larmor frequency (64-300MHz) because MRI was used to imaging loss tangent. A multiple Cole-Cole expression [72, 73] which is used to interpolate the spectrum of the electrical properties can be used to estimate the loss tangent at the other frequencies.

5.2.2 Additional simulation and experiments

In this study, a simulation phantom was designed that was composed of one homogeneous tissue for clarity and simplicity to observe the effect of the loss tangent. The electrical properties of the background tissue give change to RF heating [74]. The current actual pathway and current density will be determined by the entire tissue's electrical properties. Therefore, additional simulation should be performed in many situations for determining the ablation efficiency and the temperature elevation.

The analysis of the loss tangent was performed using simulations and the potential of loss tangent imaging as a tool for predicting the RF wave propagation was proposed. The remaining step is phantom experiments. Phantom or *ex vivo* tissues can be a good object to observe the effect of the loss tangent during the hyperthermia. To further validate the results of simulations, additional phantom experiments are needed.

5.3 Conductivity imaging of flow

Although the estimated conductivity map shows that the double spin echo method effectively removes the flow perturbation from the whole image, there is a limitation in acquiring the flow signal using the double spin echo sequence due to the signal nulling of flow. Therefore, balanced SSFP sequence and 2D PC sequence were proposed to estimate the flow effects. With the flow component, estimation of conductivity is inaccurate at the flow due to additional flow induced phase. The proposed process can correct for the flow related additional phase but this technique is not suitable for *in vivo* application. Also, separation of the flow induced phase from the B_1^+ phase is impracticable using only a spatial polynomial

fitting. The flow induced phase would be correlated with echo time, local field variation and other extra terms. More dedicated approaches such as interleaving the flow encoding and non-flow encoding should be provided for a more robust method.

References

1. Wen, H., *Non-invasive Quantitative Mapping of Conductivity and Dielectric Distributions Using the RF Wave Propagation Effects in High Field MRI.* Physics of Medical Imaging Proc SPIE, 2003. **5030**.
2. Katscher, U., et al., *Determination of electric conductivity and local SAR via B_1 mapping.* IEEE Trans Med Imaging, 2009. **28**(9): p. 1365-74.
3. Voigt, T., U. Katscher, and O. Doessel, *Quantitative conductivity and permittivity imaging of the human brain using electric properties tomography.* Magn Reson Med, 2011. **66**(2): p. 456-66.
4. Liang, Z.-p. and P.C. Lauterbur, *Principles of Magnetic Resonance Imaging*. IEEE Press Series in Biomedical Engineering. 2000, New York: The Institute of Electical and Electronics Engineers, Inc.
5. Glover, G.H., et al., *Comparison of Linear and Circular-Polarization for Magnetic-Resonance Imaging.* J Magn Reson, 1985. **64**(2): p. 255-270.
6. Adriany, G., et al., *A 32-channel lattice transmission line array for parallel transmit and receive MRI at 7 tesla.* Magn Reson Med, 2010. **63**(6): p. 1478-85.
7. Metzger, G.J., et al., *Performance of external and internal coil configurations for prostate investigations at 7T.* Magn Reson Med, 2010. **64**(6): p. 1625-39.
8. Lenz, C., et al., *Simultaneous B_1 and B_0 mapping using dual echo actual flip angle imaging (DE-AFI).* Proc ISMRM, 2011: p. 4408.
9. Venkatesan, R., W. Lin, and E.M. Haacke, *Accurate determination of spin-density and T_1 in the presence of RF-field inhomogeneities and flip-angle miscalibration.* Magn Reson Med, 1998. **40**(4): p. 592-602.
10. Deoni, S.C., *High-resolution T_1 mapping of the brain at 3T with driven equilibrium single pulse observation of T_1 with high-speed incorporation of RF field inhomogeneities (DESPOT1-HIFI).* J Magn Reson Imaging, 2007. **26**(4): p. 1106-11.
11. Gilbert, K.M., et al., *A radiofrequency coil to facilitate B_1^+ shimming and parallel imaging acceleration in three dimensions at 7T.* NMR Biomed, 2011. **24**(7): p. 815-23.
12. Stollberger, R. and P. Wach, *Imaging of the active B_1 field in vivo.* Magn Reson Med, 1996. **35**(2): p. 246-51.
13. Nehrke, K., *On the steady-state properties of actual flip angle imaging (AFI).* Magn Reson Med, 2009. **61**(1): p. 84-92.
14. Cunningham, C.H., J.M. Pauly, and K.S. Nayak, *Saturated double-angle method for rapid B_1^+ mapping.* Magn Reson Med, 2006. **55**(6): p. 1326-33.
15. Sacolick, L.I., et al., *B_1 mapping by Bloch-Siegert shift.* Magn Reson Med, 2010. **63**(5): p. 1315-22.
16. Nehrke, K. and P. Bornert, *DREAM-a novel approach for robust, ultrafast, multislice B_1 mapping.* Magn Reson Med, 2012. **68**(5): p. 1517-26.
17. Yarnykh, V.L., *Actual flip-angle imaging in the pulsed steady state: a method for rapid three-dimensional mapping of the transmitted radiofrequency field.* Magn Reson Med, 2007. **57**(1): p. 192-200.

18. Akoka, S., et al., *Radiofrequency map of an NMR coil by imaging.* Magn Reson Imaging, 1993. **11**(3): p. 437-41.
19. Dowell, N.G. and P.S. Tofts, *Fast, accurate, and precise mapping of the RF field in vivo using the 180 degrees signal null.* Magn Reson Med, 2007. **58**(3): p. 622-30.
20. Voigt, T., et al., *T_1 corrected B_1 mapping using multi-TR gradient echo sequences.* Magn Reson Med, 2010. **64**(3): p. 725-33.
21. Morrell, G.R., *A phase-sensitive method of flip angle mapping.* Magn Reson Med, 2008. **60**(4): p. 889-94.
22. Jordanova, K.V., D.G. Nishimura, and A.B. Kerr, *B_1 estimation using adiabatic refocusing: BEAR.* Magn Reson Med, 2014. **72**(5): p. 1302-10.
23. Yang, Q.X., et al., *Analysis of wave behavior in lossy dielectric samples at high field.* Magn Reson Med, 2002. **47**(5): p. 982-9.
24. Wang, J., et al., *Measurement and correction of transmitter and receiver induced nonuniformities in vivo.* Magn Reson Med, 2005. **53**(2): p. 408-17.
25. Shin, J., et al., *Quantification Error in MREPT due to B_1 Map Inaccuracy.* Proc ISMRM, 2012: p. 2533.
26. van Lier, A.L., et al., *B_1^+ phase mapping at 7T and its application for in vivo electrical conductivity mapping.* Magn Reson Med, 2012. **67**(2): p. 552-61.
27. Hoult, D.I., *The principle of reciprocity in signal strength calculations - A mathematical guide.* Concepts Magn Reson, 2000. **12**(4): p. 173-187.
28. Zhang, X., et al., *From complex B_1 mapping to local SAR estimation for human brain MR imaging using multi-channel transceiver coil at 7T.* IEEE Trans Med Imaging, 2013. **32**(6): p. 1058-67.
29. Gabriel, S., R.W. Lau, and C. Gabriel, *The dielectric properties of biological tissues: II. Measurements in the frequency range 10 Hz to 20 GHz.* Phys Med Biol, 1996. **41**(11): p. 2251-69.
30. Schmid, G., G. Neubauer, and P.R. Mazal, *Dielectric properties of human brain tissue measured less than 10 h postmortem at frequencies from 800 to 2450 MHz.* Bioelectromagnetics, 2003. **24**(6): p. 423-30.
31. Peyman, A., et al., *Dielectric properties of porcine cerebrospinal tissues at microwave frequencies: in vivo, in vitro and systematic variation with age.* Phys Med Biol, 2007. **52**(8): p. 2229-45.
32. Visser, K.R., *Electric properties of flowing blood and impedance cardiography.* Ann Biomed Eng, 1989. **17**(5): p. 463-73.
33. Haemmerich, D., et al., *In vivo electrical conductivity of hepatic tumours.* Physiol Meas, 2003. **24**(2): p. 251-60.
34. Chauhan, M., et al., *Radiofrequency ablation lesion detection using MR-based electrical conductivity imaging: a feasibility study of ex vivo liver experiments.* Int J Hyperthermia, 2013. **29**(7): p. 643-52.
35. Oh, T.I., et al., *Feasibility of magnetic resonance electrical impedance tomography (MREIT) conductivity imaging to evaluate brain abscess lesion: in vivo canine model.* J Magn Reson Imaging, 2013. **38**(1): p. 189-97.
36. Gabriel, C., S. Gabriel, and E. Corthout, *The dielectric properties of biological tissues: I. Literature survey.* Phys Med Biol, 1996. **41**(11): p. 2231-49.
37. Oh, T.I., et al., *Ion mobility imaging and contrast mechanism of apparent conductivity in MREIT.* Phys Med Biol, 2011. **56**(7): p. 2265-77.

38. Kim, D.H., et al., *Frequency-Dependent Conductivity Contrast for Tissue Characterization Using a Dual-Frequency Range Conductivity Mapping Magnetic Resonance Method.* IEEE Trans Med Imaging, 2014. doi: 10.1109/TMI.2014.2361689
39. Seo, J.K., et al., *Error analysis of nonconstant admittivity for MR-based electric property imaging.* IEEE Trans Med Imaging, 2012. **31**(2): p. 430-7.
40. Kim, H.J., et al., *Simultaneous imaging of dual-frequency electrical conductivity using a combination of MREIT and MREPT.* Magn Reson Med, 2014. **71**(1): p. 200-8.
41. Hoetink, A.E., et al., *On the flow dependency of the electrical conductivity of blood.* IEEE Trans Biomed Eng, 2004. **51**(7): p. 1251-61.
42. Schar, M., E.J. Vonken, and M. Stuber, *Simultaneous B_0- and B_1^+-map acquisition for fast localized shim, frequency, and RF power determination in the heart at 3T.* Magn Reson Med, 2010. **63**(2): p. 419-26.
43. Voigt, T., et al., *Patient-individual local SAR determination: in vivo measurements and numerical validation.* Magn Reson Med, 2012. **68**(4): p. 1117-26.
44. Underhill, H.R., C. Yuan, and C.E. Hayes, *A combined solenoid-surface RF coil for high-resolution whole-brain rat imaging on a 3.0 Tesla clinical MR scanner.* Magn Reson Med, 2010. **64**(3): p. 883-92.
45. Sled, J.G. and G.B. Pike, *Correction for B_1 and B_0 variations in quantitative T_2 measurements using MRI.* Magn Reson Med, 2000. **43**(4): p. 589-93.
46. Cheng, H.L. and G.A. Wright, *Rapid high-resolution T_1 mapping by variable flip angles: accurate and precise measurements in the presence of radiofrequency field inhomogeneity.* Magn Reson Med, 2006. **55**(3): p. 566-74.
47. Haacke, E.M., et al., *Extraction of Conductivity and Permittivity Using Magnetic-Resonance-Imaging.* Phys Med Biol, 1991. **36**(6): p. 723-734.
48. Zhang, X., et al., *Complex B_1 mapping and electrical properties imaging of the human brain using a 16-channel transceiver coil at 7T.* Magn Reson Med, 2013. **69**(5): p. 1285-96.
49. Amadon, A. and N. Boulant, *Simultaneous measurement of B_0- and B_1-maps with modified Actual Flip Angle Imaging sequence.* Proc ISMRM, 2008: p. 1248.
50. Jenkinson, M., *Fast, automated, N-dimensional phase-unwrapping algorithm.* Magn Reson Med, 2003. **49**(1): p. 193-7.
51. Peran, P., et al., *Voxel-based analysis of R_2* maps in the healthy human brain.* J Magn Reson Imaging, 2007. **26**(6): p. 1413-20.
52. Guiu, B., et al., *Quantification of liver fat content: comparison of triple-echo chemical shift gradient-echo imaging and in vivo proton MR spectroscopy.* Radiology, 2009. **250**(1): p. 95-102.
53. Shultz, K., et al., *RF field visualization of RF ablation at the Larmor frequency.* IEEE Trans Med Imaging, 2012. **31**(4): p. 938-47.
54. Gruetter, R. and C. Boesch, *Fast, Noniterative Shimming of Spatially Localized Signals - Invivo Analysis of the Magnetic-Field Along Axes.* J Magn Reson, 1992. **96**(2): p. 323-334.
55. Terpstra, M., P.M. Andersen, and R. Gruetter, *Localized eddy current compensation using quantitative field mapping.* J Magn Reson, 1998. **131**(1): p. 139-43.

56. Spees, W.M., et al., *Quantification and compensation of eddy-current-induced magnetic-field gradients.* J Magn Reson, 2011. **212**(1): p. 116-23.
57. Brace, C.L., *Microwave tissue ablation: biophysics, technology, and applications.* Crit Rev Biomed Eng, 2010. **38**(1): p. 65-78.
58. Garrean, S., et al., *Radiofrequency ablation of primary and metastatic liver tumors: a critical review of the literature.* Am J Surg, 2008. **195**(4): p. 508-20.
59. Goldberg, S.N., et al., *Image-guided tumor ablation: standardization of terminology and reporting criteria.* J Vasc Interv Radiol, 2009. **20**(7 Suppl): p. S377-90.
60. Haemmerich, D., *Biophysics of radiofrequency ablation.* Crit Rev Biomed Eng, 2010. **38**(1): p. 53-63.
61. van der Put, R.W., et al., *Contour propagation in MRI-guided radiotherapy treatment of cervical cancer: the accuracy of rigid, non-rigid and semi-automatic registrations.* Phys Med Biol, 2009. **54**(23): p. 7135-50.
62. McDannold, N., et al., *Transcranial magnetic resonance imaging- guided focused ultrasound surgery of brain tumors: initial findings in 3 patients.* Neurosurgery, 2010. **66**(2): p. 323-32.
63. Fuentes, D., et al., *Magnetic resonance temperature imaging validation of a bioheat transfer model for laser-induced thermal therapy.* Int J Hyperthermia, 2011. **27**(5): p. 453-64.
64. Hynynen, K., et al., *MR imaging-guided focused ultrasound surgery of fibroadenomas in the breast: a feasibility study.* Radiology, 2001. **219**(1): p. 176-85.
65. Peyman, A., et al., *Dielectric properties of human placenta, umbilical cord and amniotic fluid.* Phys Med Biol, 2011. **56**(7): p. N93-8.
66. van den Bergen, B., et al., *Ultra fast electromagnetic field computations for RF multi-transmit techniques in high field MRI.* Phys Med Biol, 2009. **54**(5): p. 1253-64.
67. Choi, N., et al., *A modified multi-echo AFI for simultaneous B_1^+ magnitude and phase mapping.* Magn Reson Imaging, 2014. **32**(4): p. 314-20.
68. Renou, R., et al., *Concentration dependence of the dielectric permittivity, structure, and dynamics of aqueous NaCl solutions: comparison between the Drude oscillator and electronic continuum models.* J Phys Chem B, 2014. **118**(14): p. 3931-40.
69. Akilan, C., *Thermodynamic and related studies of aqueous copper (II) sulfate solutions.* Ph.D. Dissertation. Australia: Murdoch Univ., 2008: p. 87-134.
70. Weast, R.C., M.J. Astle, and W.H. Beyer, *CRC Handbook of Chemistry and Physics*. . 1988-1989, Boca Raton, Florida: CRC Press, Inc.
71. Wolf, A.V., *Aqueous solutions and body fluids; their concentrative properties and conversion tables*. 1966, New York,: Hoeber Medical Division. xiv, 166 p.
72. Cole, K.S. and R.H. Cole, *Dispersion and Absorption in Dielectrics I. Alternating Current Characteristics.* J Chem Phys, 1941. **9**: p. 341.
73. Peyman, A. and C. Gabriel, *Cole-Cole parameters for the dielectric properties of porcine tissues as a function of age at microwave frequencies.* Phys Med Biol, 2010. **55**(15): p. N413-9.
74. Solazzo, S.A., et al., *Radiofrequency ablation: importance of background tissue electrical conductivity--an agar phantom and computer modeling study.* Radiology, 2005. **236**(2): p. 495-502.

75. Huang, L., et al., *A Monte Carlo method for overcoming the edge artifacts in MRI-based electrical conductivity mapping.* Proc ISMRM, 2014: p. 3190.
76. Geddes, L.A. and L.E. Baker, *The specific resistance of biological material--a compendium of data for the biomedical engineer and physiologist.* Med Biol Eng, 1967. **5**(3): p. 271-93.
77. Kubicek, W.G., et al., *Development and evaluation of an impedance cardiac output system.* Aerosp Med, 1966. **37**(12): p. 1208-12.
78. Geddes, L.A. and C. Sadler, *The specific resistance of blood at body temperature.* Med Biol Eng, 1973. **11**(3): p. 336-9.
79. Hirsch, F.G., et al., *The electrical conductivity of blood. I: Relationship to erythrocyte concentration.* Blood, 1950. **5**(11): p. 1017-35.
80. Fricke, H., *The Electric Capacity of Suspensions with Special Reference to Blood.* J Gen Physiol, 1925. **9**(2): p. 137-52.
81. Dellimore, J.W. and R.G. Gosling, *Change in blood conductivity with flow rate.* Med Biol Eng, 1975. **13**(6): p. 904-13.
82. Bernstein, M.A., A. Shimakawa, and N.J. Pelc, *Minimizing TE in moment-nulled or flow-encoded two- and three-dimensional gradient-echo imaging.* J Magn Reson Imaging, 1992. **2**(5): p. 583-8.
83. Wood, M.L., Y. Zur, and L.J. Neuringer, *Gradient moment nulling for steady-state free precession MR imaging of cerebrospinal fluid.* Med Phys, 1991. **18**(5): p. 1038-44.
84. Hinks, R.S. and R.T. Constable, *Gradient moment nulling in fast spin echo.* Magn Reson Med, 1994. **32**(6): p. 698-706.
85. Ahn, C.B., et al., *The effects of random directional distributed flow in nuclear magnetic resonance imaging.* Med Phys, 1987. **14**(1): p. 43-8.
86. Lotz, J., et al., *Cardiovascular flow measurement with phase-contrast MR imaging: basic facts and implementation.* Radiographics, 2002. **22**(3): p. 651-71.
87. Moran, P.R., R.A. Moran, and N. Karstaedt, *Verification and evaluation of internal flow and motion. True magnetic resonance imaging by the phase gradient modulation method.* Radiology, 1985. **154**(2): p. 433-41.
88. Bryant, D.J., et al., *Measurement of flow with NMR imaging using a gradient pulse and phase difference technique.* J Comput Assist Tomogr, 1984. **8**(4): p. 588-93.
89. Xu, B., et al., *Flow compensated quantitative susceptibility mapping for venous oxygenation imaging.* Magn Reson Med, 2014. **72**(2): p. 438-45.
90. Gaw, R.L., B.H. Cornish, and B.J. Thomas, *Comparison of a theoretical impedance model with experimental measurements of pulsatile blood flow.* IFMBE Proc., 2007. **17**: p. 32-35.
91. Frahm, J., K.D. Merboldt, and W. Hanicke, *Direct FLASH MR imaging of magnetic field inhomogeneities by gradient compensation.* Magn Reson Med, 1988. **6**(4): p. 474-80.
92. Choi, N., et al., *In vivo conductivity mapping using double spin echo for flow effect removal.* Proc ISMRM, 2011: p. 4466.

국문요약

자기공명영상장치는 인체 내부를 방사능 피폭 없이 비침습적으로 시각화 할 수 있으며 임상적으로 매우 유용하게 이용된다. 특히 다양한 대조도의 영상을 제공하며 다양한 활용성으로 인하여 기초과학연구분야에서도 많은 연구가 진행되고 있다. 자기공명영상을 이용한 다양한 정량분석연구 중에 생체 내의 전기적 특성에 대한 영상화 연구는 비교적 최근에 등장한 분야이다. 생체 내의 전기적 특성은 다양한 분야에서 활용될 수 있으나 기존의 연구들은 침습적인 방식를 통해 이루어졌기 때문에 임상적 이용에 한계가 있다. 따라서 본 논문은 생체 내의 전기적 특성을 자기공명영상을 이용하여 측정하는 방법을 소개하며 전기적 특성을 이용한 새로운 대조도의 영상을 제시한다. 첫째로 생체 내의 전기적 특성을 측정하기 위해 사용되는 신호를 자기공명영상장치로부터 획득하는 방법을 개발하였다. 기존의 방법보다 개선된 신호를 획득하며 동시에 크기영상과 위상영상을 획득함으로써 스캔 시간을 단축하였다. 둘째로 획득한 도전율과 유전율 영상을 통해 새로운 대조도를 가지는 로스 탄젠트 영상을 제시하였으며 로스 탄젠트 영상의 특성과 활용 분야에 대해 분석하였다. 마지막으로 기존 방식으로 제거하기 힘들었던 유체의 영향을 도전율 영상으로부터 제거하였으며 유체의 도전율을 획득하기 위한 기법을 제시하였다. 이상의 연구성과들은 기존에 침습적으로 수행되던 정량분석연구분야를 비침습적인 연구를 통해 수행할 수 있도록 하며 자기공명영상 연구분야를 확장시키는 데에 기여할 수 있을 것이다.

핵심용어: 자기공명영상, 외부자장 지도화, 전기적 특성 지도화, 도전율 영상, 유전율 영상, 로스 탄젠트 영상, 유체 영향 제거